

On the use of eddy viscosity in resolvent analysis of turbulent channel flow

Sean Symon*

*Aerodynamics and Flight Mechanics, Faculty of Engineering and Physical Sciences,
University of Southampton, SO17 1BJ, United Kingdom*

Anagha Madhusudanan

*Department of Applied Mathematics and Theoretical Physics, Centre for Mathematical Sciences,
University of Cambridge, Cambridge CB3 0WA, United Kingdom*

Simon J. Illingworth and Ivan Marusic

*Department of Mechanical Engineering, University of Melbourne, Parkville, VIC 3010, Australia
(Dated: May 24, 2022)*

The predictions of resolvent analysis for turbulent channel flow are evaluated for a friction Reynolds number of $Re_\tau = 550$. In addition to the standard resolvent operator where only the kinematic viscosity appears, a resolvent operator augmented with the Cess eddy viscosity profile is considered. Adding eddy viscosity significantly alters the low-rank behavior of the resolvent. Regardless of the wave speed selected, the eddy resolvent is low-rank for spanwise wavelengths of $\lambda_y^+ = 80$ and $\lambda_y/h = 3.5$ in comparison to the standard resolvent whose low-rank behavior depends on the wave speed. The leading eddy resolvent modes are shown to have higher projections onto the leading mode from spectral proper orthogonal decomposition in comparison to standard resolvent modes. Neither analysis, however, reliably predicts the most energetic wave speed. The standard resolvent tends to overestimate it while the eddy resolvent underestimates it. For scales where the most energetic wave speed is underestimated, the eddy resolvent modes are energetic too close to the wall. The eddy resolvent does, however, correctly identify the most energetic wave speed and mode shapes for structures that are associated with the near-wall cycle or that are most energetic at $z/h = \pm 0.5$. It is argued that these types of structures are likely to be correctly predicted for any friction Reynolds number due to the inner and outer scaling of the Cess eddy viscosity profile. Finally, it is shown that the accuracy of eddy predictions relies on striking the right balance between positive and negative energy transfers. Even though the eddy viscosity primarily adds dissipation, its wall-normal gradient injects energy in the near-wall region, resulting in mode shapes that are “attached” to the wall. For some scales, however, the predicted positive energy transfer is too strong thus biasing structures towards the wall. The ability of the Cess eddy viscosity profile to model both positive and negative energy transfers suggests that it could be optimized for individual scales to provide better low-order models of turbulent channel flow.

I. INTRODUCTION

The Navier-Stokes equations linearized around the mean (time-averaged) flow have been used to identify coherent structures in a variety of flows. In the resolvent-based approach of Ref. [1], for example, the linearized Navier-Stokes equations are analyzed from an input-output perspective. The input is made up of nonlinear perturbation terms that are treated as an intrinsic forcing to the linear resolvent operator and the output is the perturbation velocity field. In the context of wall-bounded flows, resolvent analysis has been exploited for a variety of applications from finding reduced-order models of exact coherent states [2] to predicting statistics of high-Reynolds-number turbulence [3, 4]. The ability of resolvent analysis to identify prominent linear mechanisms, moreover, has made it an attractive alternative to direct numerical simulation (DNS) for designing flow control strategies [5–7].

From DNS and experimental studies of wall-bounded flows, it is known that the production of turbulent kinetic energy is mainly driven by the exchange of energy from the mean flow to the fluctuations. Resolvent

* sean.symon@soton.ac.uk

analysis models well this exchange from the mean to the fluctuations, where the mean is assumed to be known *a priori*. Therefore, the term in the energy budget that the resolvent analysis captures most successfully is production [8, 9]. The resolvent operator also tends to be low-rank for energy-producing scales [3]. The term that resolvent analysis captures the least accurately for an arbitrary scale is nonlinear transfer between scales. One way to model this term is to add an eddy viscosity to the resolvent operator [10–16]. The eddy viscosity provides additional dissipation that removes energy from all scales. As such, it attempts to model this nonlinear transfer of energy from the large scales to the small scales.

In terms of structures, many studies have observed good agreement between the structures predicted by resolvent analysis, and those found in DNS. The leading resolvent mode, which is computed as the leading left singular vector of the resolvent operator, is the dominant structure predicted by resolvent analysis. The dominant mode from DNS is computed as the leading mode from spectral proper orthogonal decomposition (SPOD) [17, 18]. In fact, if the nonlinear forcing is white in space and time, then resolvent and SPOD modes are theoretically equivalent [19]. The nonlinear forcing, however, is not white in space and time [15, 20, 21]. As such, the role of eddy viscosity is to model the effect of the nonlinear forcing such that white in space and time forcing is sufficient to predict the correct structures. Reference [13] showed that adding eddy viscosity improved predictions of coherent motions in turbulent channel flow at a friction Reynolds number of $Re_\tau = 1007$. However, they only considered the streamwise velocity component of two of the energetic scales in the flow. Reference [22] compared resolvent predictions with and without eddy viscosity for turbulent channel flow at $Re_\tau = 2003$. The study was limited, however, to temporal snapshots of the largest scales. The most comprehensive comparison between resolvent and SPOD modes has been presented by Ref. [23], who computed the projection of the leading resolvent mode onto the leading SPOD mode for turbulent pipe flow at low Reynolds numbers. The authors noted good agreement, i.e. high projections between the resolvent and SPOD modes, for scales where the lift-up mechanism [24, 25] was active. They did not, however, consider the improvements that could be achieved by adding an eddy viscosity model as done by Ref. [26].

A rigorous comparison of resolvent and SPOD modes across all scales and wave speeds, therefore, is needed for resolvent analysis with and without eddy viscosity. As such, one of the principal objectives of this article is to quantify the projections of the leading resolvent mode computed with and without eddy viscosity onto the leading SPOD mode. Previous work [22] suggests that analyzing the accuracy with which the resolvent model predicts the wave speed at which a structure convects is crucial when comparing the model predictions with DNS. This motivates the second objective of this work which is to perform a detailed analysis of the most amplified wave speeds identified by resolvent analysis with and without eddy viscosity and how they compare to the most energetic wave speed computed from DNS. The most energetic wave speed of a structure is also indicative of the wall-normal location where most of its energy is concentrated and, therefore, of the shape of the mode in the wall-normal direction. The final objective of this article is to provide insight into the types of nonlinear interactions that the eddy viscosity is attempting to model. As mentioned earlier, the eddy viscosity primarily adds extra dissipation to the energy balance, but its wall-normal gradient has been shown to add energy overall to a scale [8]. It is worth examining the wall-normal profiles of the transfers introduced by eddy viscosity to determine if they model the positive energy transfer in the near-wall region that has been observed in DNS for large scales [27–30].

The rest of the paper is organised as follows. Section II presents the governing equations for channel flow and provides a brief overview of resolvent analysis, the Cess eddy viscosity profile, and SPOD. The details of the DNS for $Re_\tau = 550$ are provided in Sec. III. The predictions of resolvent and eddy analysis are evaluated in Sec. IV using scalar quantities. These include the ratio of energy contained in the first pair of singular values compared to the total energy, the projections of the leading resolvent modes onto the leading SPOD modes, and comparing the most amplified wave speed from resolvent analysis to the most energetic wave speed in DNS. Section V provides a more detailed comparison of the mode shapes for select scales. The extent to which a constant eddy viscosity profile, i.e. one that does not depend on space, can successfully predict structures is also investigated in Sec. V. The energy transfer processes introduced by eddy viscosity are discussed in Sec. VI. The role of the eddy viscosity gradient, in particular, is examined and artificially manipulated to understand its influence on the mode shapes. Finally, conclusions and implications for optimizing a scale-dependent eddy viscosity are suggested in Sec. VII.

II. METHODOLOGY

Section II A describes the governing equations for plane Poiseuille flow and their non-dimensionalization. A brief overview of resolvent analysis is provided in Sec. II B. In Sec. II C, a modified resolvent operator, which includes the Cess eddy viscosity profile, is formulated. In order to assess the predictive capability of resolvent analysis with and without eddy viscosity, the leading modes are compared to SPOD modes, which are computed using the procedure summarized in Sec. II D.

A. Plane Poiseuille flow equations

The non-dimensional Navier-Stokes equations for statistically steady, turbulent plane Poiseuille flow are

$$\frac{\partial \mathbf{u}}{\partial t} + \mathbf{u} \cdot \nabla \mathbf{u} = -\nabla p + \frac{1}{Re_\tau} \nabla^2 \mathbf{u}, \quad (1a)$$

$$\nabla \cdot \mathbf{u} = 0, \quad (1b)$$

where $\mathbf{u}(\mathbf{x}, t) = [u, v, w]^T$ is the velocity in the x (streamwise), y (spanwise), and z (wall-normal) directions, $p(\mathbf{x}, t)$ is the pressure, and $\nabla = [\partial/\partial x, \partial/\partial y, \partial/\partial z]^T$. The friction Reynolds number $Re_\tau = u_\tau h/\nu$ is defined in terms of the friction velocity u_τ , channel half height h , and kinematic viscosity ν . Periodic boundary conditions are applied in the streamwise and spanwise directions and no-slip boundary conditions are imposed at the walls. The velocities are non-dimensionalized by u_τ , the spatial variables by h , and the pressure by ρu_τ^2 where ρ is the density of the fluid. A ‘+’ superscript denotes spatial variables that have been normalized by the viscous length scale ν/u_τ .

B. Resolvent analysis

Equation (1) is Reynolds-decomposed leading to the following equations for the fluctuations:

$$\frac{\partial \mathbf{u}'}{\partial t} + \mathbf{U} \cdot \nabla \mathbf{u}' + \mathbf{u}' \cdot \nabla \mathbf{U} + \nabla p' - \frac{1}{Re_\tau} \nabla^2 \mathbf{u}' = -\mathbf{u}' \cdot \nabla \mathbf{u}' + \overline{\mathbf{u}' \cdot \nabla \mathbf{u}'} = \mathbf{f}', \quad (2a)$$

$$\nabla \cdot \mathbf{u}' = 0, \quad (2b)$$

where $\overline{(\cdot)}$ and $(\cdot)'$ denote a time-average and fluctuation, respectively. The mean velocity profile $\mathbf{U} = [U(z), 0, 0]^T$ is assumed to be known *a priori* from DNS. Equation (2) is written such that all linear terms appear on the left-hand side. The nonlinear terms on the right-hand side are lumped together as a forcing \mathbf{f}' . Equation (2) is Laplace-transformed in time and Fourier-transformed in the homogeneous directions x and y

$$\hat{\mathbf{u}}(k_x, k_y, s) = \frac{1}{(2\pi)^3} \int_{-\infty}^{\infty} \int_{-\infty}^{\infty} \int_{-\infty}^{\infty} \mathbf{u}'(x, y, z, t) e^{st - ik_x x - ik_y y} dx dy dt. \quad (3)$$

Upon integration of Eq. (3), we set $s = i\omega$ to consider the frequency response $\hat{\mathbf{u}}(\mathbf{k})$ where (\cdot) denotes the Fourier-transformed coefficient and the wavenumber triplet $\mathbf{k} = (k_x, k_y, \omega)$ consists of streamwise wavenumber k_x , spanwise wavenumber k_y , and temporal frequency ω . The equivalent wavelengths in the streamwise and spanwise directions are $\lambda_x = 2\pi/k_x$ and $\lambda_y = 2\pi/k_y$. The wavenumbers are non-dimensionalized by $(1/h)$ and the wavelengths by h .

Equation (3) is substituted into Eq. (2) and rearranged into state-space form [31]

$$i\omega \hat{\mathbf{q}}(\mathbf{k}) = \mathbf{A}(k_x, k_y) \hat{\mathbf{q}}(\mathbf{k}) + \mathbf{B}(k_x, k_y) \hat{\mathbf{f}}(\mathbf{k}), \quad (4a)$$

$$\hat{\mathbf{u}}(\mathbf{k}) = \mathbf{C}(k_x, k_y) \hat{\mathbf{q}}(\mathbf{k}), \quad (4b)$$

where the state $\hat{\mathbf{q}}$ consists of the wall-normal velocity \hat{w} and wall-normal vorticity $\hat{\eta} = ik_y \hat{u} - ik_x \hat{v}$. The matrices \mathbf{A} , \mathbf{B} , and \mathbf{C} are the discretized forms of the linearized Navier-Stokes operator, the forcing operator and the output operator, respectively, and are defined in the Appendix. It is worth noting that \mathbf{A} , \mathbf{B} , and \mathbf{C} are independent of ω but are functions of the wavenumber pair (k_x, k_y) under consideration. For the sake of brevity, this dependence is omitted for the rest of the paper.

Equation (4) is recast into input-output form

$$\hat{\mathbf{u}}(\mathbf{k}) = \mathbf{C}(i\omega\mathbf{I} - \mathbf{A})^{-1}\hat{\mathbf{f}}(\mathbf{k}) = \mathcal{H}(\mathbf{k})\hat{\mathbf{f}}(\mathbf{k}), \quad (5)$$

where $\mathcal{H}(\mathbf{k})$ is a linear operator called the resolvent that relates the input forcing $\hat{\mathbf{f}}(\mathbf{k})$ to the output velocity $\hat{\mathbf{u}}(\mathbf{k})$. Even if $\hat{\mathbf{f}}(\mathbf{k})$ is unknown, the resolvent operator can be characterized by the singular value decomposition

$$\mathcal{H}(\mathbf{k}) = \hat{\Psi}(\mathbf{k})\Sigma(\mathbf{k})\hat{\Phi}^*(\mathbf{k}), \quad (6)$$

where $\hat{\Psi}(\mathbf{k}) = [\hat{\psi}_1(\mathbf{k}), \hat{\psi}_2(\mathbf{k}), \dots, \hat{\psi}_p(\mathbf{k})]$ are the resolvent modes, which form an orthogonal basis for velocity, and $\hat{\Phi}(\mathbf{k}) = [\hat{\phi}_1(\mathbf{k}), \hat{\phi}_2(\mathbf{k}), \dots, \hat{\phi}_p(\mathbf{k})]$ are the resolvent forcing modes which form an orthogonal basis for the nonlinear forcing. $\Sigma(\mathbf{k})$ is a diagonal matrix that ranks the p th structure by its gain $\sigma_p(\mathbf{k})$ using an inner product that is proportional to its kinetic energy, i.e. $\langle \hat{\psi}, \hat{\psi} \rangle = \int_{-h}^h \hat{\psi}^* \cdot \hat{\psi} dz$. The structure $\hat{\psi}_1(\mathbf{k})$ is, therefore, referred to as the optimal or leading resolvent mode and is the most amplified response of the linear dynamics contained in the resolvent.

The true velocity field from experiments or DNS can be expressed as a weighted sum of resolvent modes

$$\hat{\mathbf{u}}(\mathbf{k}) = \sum_{p=1}^N \hat{\psi}_p(\mathbf{k}) \sigma_p(\mathbf{k}) \chi_p(\mathbf{k}), \quad (7)$$

where $\chi_p(\mathbf{k})$ is the projection of $\hat{\phi}_p(\mathbf{k})$ onto $\hat{\mathbf{f}}(\mathbf{k})$, i.e.

$$\chi_p(\mathbf{k}) = \langle \hat{\mathbf{f}}(\mathbf{k}), \hat{\phi}_p(\mathbf{k}) \rangle. \quad (8)$$

It can be noted from Eqs. (7) and (8) that if $\hat{\mathbf{f}}(\mathbf{k})$ is white noise or projects equally onto the resolvent forcing modes, then the contribution of a resolvent mode $\hat{\psi}_p$ in reconstructing the velocity field according to Eq. (7) is solely dependent on the associated singular value σ_p . Moreover, if $\sigma_1 \gg \sigma_2$, then it is often argued that the velocity response can be well-approximated by the leading resolvent response mode $\hat{\psi}_1$ alone.

C. Cess eddy viscosity model

It has been shown, however, that the nonlinear forcing may have little to no overlap with the leading forcing mode [8, 15, 32] resulting in $\chi_1 \ll \chi_{p \neq 1}$. This nonalignment stems from the fact that the resolvent does not model well the inter-scale nonlinear transfer. To address this shortcoming, an eddy viscosity can be added to the linearized Navier-Stokes equations after performing a triple decomposition of the total velocity field $\tilde{\mathbf{u}}$ into a mean component \mathbf{U} , coherent motions \mathbf{u} , and incoherent fluctuations \mathbf{u}' [10]. A new set of equations govern the coherent velocity and pressure:

$$\frac{\partial \mathbf{u}}{\partial t} + \mathbf{U} \cdot \nabla \mathbf{u} + \mathbf{u} \cdot \nabla \mathbf{U} + \nabla p + \nabla \cdot [\nu_T(\nabla \mathbf{u} + \nabla \mathbf{u}^T)] = \mathbf{d}, \quad (9)$$

where $\nu_T(z)$ is the total effective viscosity and $\mathbf{d} = -\mathbf{u} \cdot \nabla \mathbf{u} + \overline{\mathbf{u} \cdot \nabla \mathbf{u}}$ is the disturbance term. Similar to Refs. [33] and [12], the Cess [34] eddy viscosity profile

$$\nu_T(z) = \frac{\nu}{2} \left(1 + \left[\frac{\kappa}{3} (1 - z^2)(1 + 2z^2)(1 - \exp(|z - 1|Re_\tau/A)) \right]^2 \right)^{1/2} + \frac{\nu}{2}, \quad (10)$$

is employed in this study. The constants $\kappa = 0.426$ and $A = 25.4$ are chosen based on a least-squares fit to experimental mean velocity profiles at $Re_\tau = 2000$ [35]. Even though the Reynolds number in this study is

Re_τ	L_x	L_y	L_z	N_x	N_y	N_z	Δx^+	Δy^+	Δz_{min}^+	Δz_{max}^+
550	2π	π	$2h$	256	256	201	13.5	6.75	6.79×10^{-2}	8.64

TABLE I. Channel flow DNS parameters.

lower than the Reynolds number for which the fit was performed, it has been verified that the results are not sensitive to the values of these constants.

As done in Sec. II B, Eq. (9) is Fourier-transformed in time and the homogeneous directions to obtain an input-output relationship between the velocity and disturbance fields

$$\hat{\mathbf{u}}(\mathbf{k}) = \mathcal{H}^e(\mathbf{k})\hat{\mathbf{d}}(\mathbf{k}), \quad (11)$$

where $\mathcal{H}^e(\mathbf{k})$ is a modified resolvent operator. Its singular value decomposition can be written as

$$\mathcal{H}^e(\mathbf{k}) = \hat{\Psi}^e(\mathbf{k})\Sigma^e(\mathbf{k})\hat{\Phi}^{*,e}(\mathbf{k}). \quad (12)$$

The superscript e differentiates the eddy resolvent modes, henceforth referred to as eddy modes, and singular values from their standard resolvent counterparts in Eq. (6). The interpretation of each term in the decomposition is similar to Eq. (6) in that $\hat{\Psi}^e(\mathbf{k})$ consists of orthogonal basis functions for the velocity field and the diagonal matrix $\Sigma^e(\mathbf{k})$ ranks the p th structure by its gain using an inner product proportional to its kinetic energy. The matrix $\hat{\Phi}^e(\mathbf{k})$, on the other hand, contains orthogonal basis functions for the disturbance field $\hat{\mathbf{d}}(\mathbf{k})$ which is less interpretable than $\hat{\mathbf{f}}(\mathbf{k})$. Despite this drawback, the addition of eddy viscosity is expected to partially model the effect of $\hat{\mathbf{f}}(\mathbf{k})$ and thus improve the efficiency of eddy modes as a basis for the velocity field.

D. Spectral proper orthogonal decomposition

The efficiency of resolvent and eddy modes as a basis for the velocity field can be assessed by projecting them onto SPOD modes, which are computed directly from data. The SPOD modes are computed with the same procedure described in Ref. [19] so only a brief summary is presented here. Using Welch's method [36], the DNS data for a particular (k_x, k_y) are divided into overlapping segments containing 512 snapshots with 75% overlap. Each segment is Fourier-transformed in time and the Fourier modes for a specific frequency ω can be arranged into the new data matrix

$$\hat{\mathbf{Q}}(\mathbf{k}) = \begin{bmatrix} \hat{\mathbf{q}}_\omega^{(1)} & \hat{\mathbf{q}}_\omega^{(2)} & \dots & \hat{\mathbf{q}}_\omega^{(s)} \end{bmatrix} \in \mathbb{C}^{m \times s}, \quad (13)$$

where m represents the number of states and s the number of segments. The cross-spectral density matrix for a specific wavenumber triplet $\hat{\mathbf{S}}(\mathbf{k})$ is

$$\hat{\mathbf{S}}(\mathbf{k}) = \hat{\mathbf{Q}}(\mathbf{k})\hat{\mathbf{Q}}^*(\mathbf{k}). \quad (14)$$

The SPOD eigenvectors (or modes) $\hat{\mathbf{V}}(\mathbf{k})$ and eigenvalues $\Lambda(\mathbf{k})$ can be obtained by performing an eigenvalue decomposition of the cross-spectral density matrix

$$\hat{\mathbf{S}}(\mathbf{k})\hat{\mathbf{V}}(\mathbf{k}) = \hat{\mathbf{V}}(\mathbf{k})\Lambda(\mathbf{k}). \quad (15)$$

III. DNS DATASET

A DNS of channel flow at $Re_\tau = 550$ is performed using the ChannelFlow pseudo-spectral code [37]. Table I summarizes the parameters of the simulation which was solved on a domain with dimensions $2\pi \times \pi \times 2h$ in the streamwise (L_x), spanwise (L_y) and wall-normal (L_z) directions. There are $N_x = N_y = 256$ equally spaced points in the streamwise and spanwise directions and $N_z = 201$ points in the wall-normal direction on a Chebyshev grid. Periodic boundary conditions are employed in the streamwise and spanwise directions while

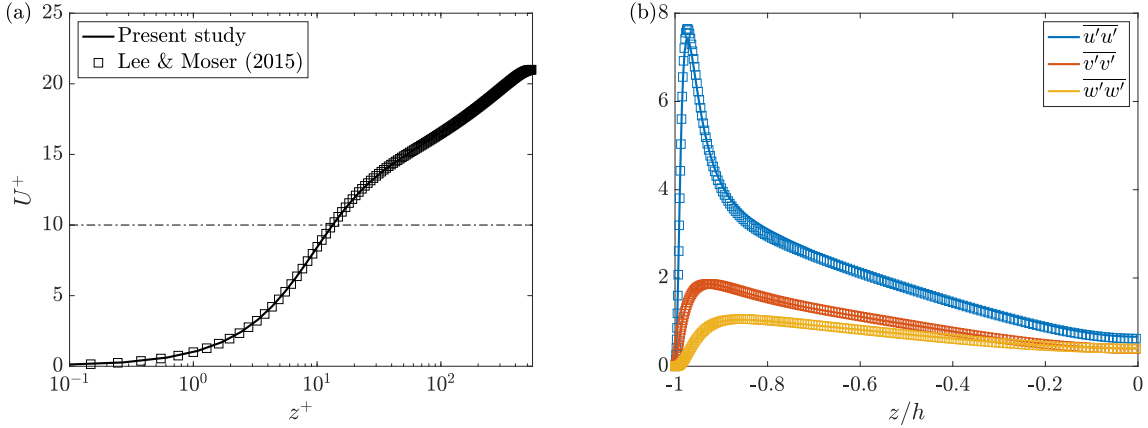


FIG. 1. (a) Mean velocity profile and (b) Reynolds stress profiles from the present study (solid lines) and Ref. [38] (open squares).

no-slip boundary conditions are enforced on the channel walls. Further details on the mesh discretization (Δx^+ , Δy^+ , Δz_{min}^+ , Δz_{max}^+) are presented in Table I. The mean velocity and Reynolds stress profiles are presented in Figs. 1(a) and (b), respectively. All profiles show good agreement with the DNS results from Ref. [38] despite the smaller computational box in this study.

SPOD is performed on a database of 6784 snapshots at a time resolution of $\Delta t = 0.2$. The data are divided into equal segments containing 512 snapshots with an overlap of 75% resulting in 50 blocks. The cross-spectral density matrices in Eq. (14) are computed using Welch's method with a Hamming window. The SPOD modes and their respective energies for a desired frequency are obtained from the eigenvectors and eigenvalues, respectively, of the cross-spectral density matrices.

IV. RESOLVENT AND EDDY ANALYSIS PREDICTIONS

In this section, the predictions from resolvent and eddy analysis, i.e. the resolvent supplemented with an eddy viscosity model, are compared to DNS data using several measures. To begin with, the low-rank behavior of the resolvent is compared to the turbulent kinetic energy spectrum of DNS in Sec. IV A. Next, the projection of the leading resolvent and eddy modes onto the dominant SPOD mode is computed in Sec. IV B for the most energetic wavenumber pairs. Structures convecting at a range of wave speeds $c^+ = \omega/k_x$ are considered, and projections are computed independently for each wave speed. In Sec. IV C, the most energetic wave speed for a range of (k_x, k_y) wavenumber pairs in DNS is compared to the most amplified wave speed identified by resolvent and eddy analysis. This motivates the selection of specific wavenumber triplets to examine in greater detail in Sec. V in which the SPOD, resolvent, and eddy mode shapes are compared directly.

A. Low-rank maps

An important aspect of the resolvent operator is its rank or, more specifically, the ratio of the total energy that is captured by the leading resolvent modes alone. Reference [3] was able to show that for a turbulent channel flow at $Re_\tau = 2003$, in the region of the (k_x, k_y) space where the real flow is energetic (as seen from experiments or DNS), the standard resolvent operator tends to be low-rank. With this observation in mind, in this section the low-rank maps from resolvent and eddy analysis are compared to the turbulent kinetic energy spectra from DNS (data provided by Refs. [39] and [40]). As noted by Ref. [3], the symmetry of the channel leads to the resolvent singular values coming in (approximately) equal pairs. One mode in each pair is symmetric with respect to the channel centerline while the other mode is anti-symmetric. The low-rank behavior of the resolvent for the channel can therefore be studied by computing the ratio of the dominant

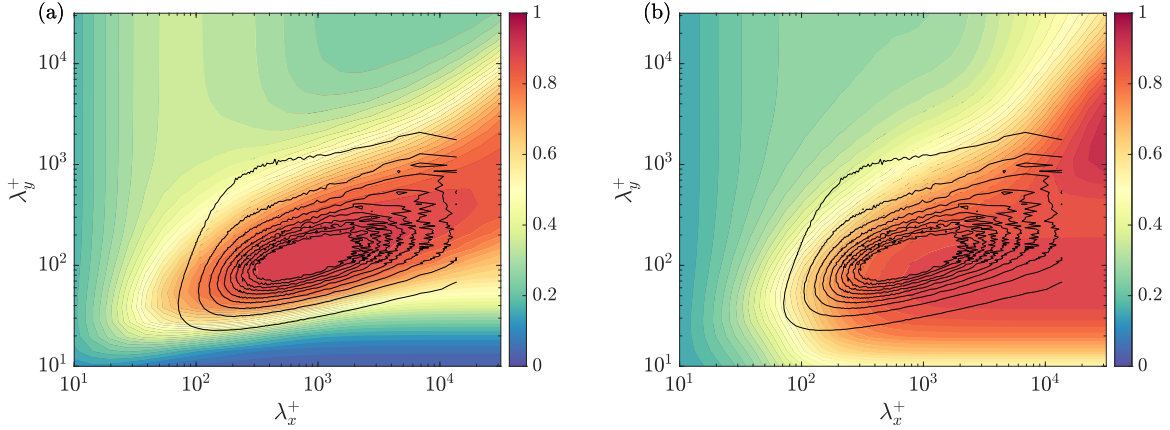


FIG. 2. Low-rank maps for (a) resolvent and (b) eddy analysis for a fixed wave speed of $c^+ = 10$. Contours of the turbulent kinetic energy spectrum at $z^+ = 15$ from Refs. [39] and [40] are denoted in black.

pair of singular values to the sum of all singular values, i.e.

$$\mathcal{R}(\mathbf{k}) = \frac{\sigma_1^2(\mathbf{k}) + \sigma_2^2(\mathbf{k})}{\sum_p \sigma_p^2(\mathbf{k})}. \quad (16)$$

Since \mathcal{R} depends on a wavenumber triplet, \mathcal{R} is computed across (λ_x, λ_y) for a fixed wave speed in order to facilitate visualization.

The low-rank maps for $c^+ = 10$ are presented in Figs. 2(a) and (b) for resolvent and eddy analysis, respectively. The wall-normal location corresponding to $U^+ = 10$ is approximately $z^+ = 15$ as indicated by the dash-dotted line in Fig. 1(a). The colours in the figure represent the value of $\mathcal{R}(\mathbf{k})$, while the black contour lines represent the streamwise turbulent kinetic energy spectrum from DNS at $z^+ \approx 15$ [39, 40]. Figure 2(a) shows that there is very good agreement between the scales with the most energy in DNS and the scales at which the resolvent is low-rank. This is to be expected since the energetic structures in the flow tend to arise from linear amplification mechanisms that are identified well by resolvent analysis [1, 31]. The eddy low-rank map in Fig. 2(b) has two main differences from its resolvent counterpart in Fig. 2(a). The first is that there is less agreement between the low-rank map and the energy spectra. The most energetic scales from DNS with spanwise wavelengths of $\lambda_y^+ \approx 100$, for example, do not coincide with the peak in the eddy low-rank map which occurs at $\lambda_y^+ \approx 80$. The second is that there are two peaks in the low-rank map for the eddy analysis whereas there is only one for resolvent analysis. The two peaks from the eddy operator occur at $\lambda_y^+ = 80$ and $\lambda_y = 3.5h$, wavelengths that have been previously observed by Refs. [35] and [12] in the context of transient growth and harmonic forcing analyses, respectively. It can be observed that there is some energy from larger scales present at this wall-normal location as attested to by the closed contour of kinetic energy centered on $(\lambda_x, \lambda_y) = (14h, 2h)$ or $(\lambda_x^+, \lambda_y^+) = (7700, 1100)$. Nevertheless, the Reynolds number of this study is too low to conclude that the second peak around $\lambda_y = 3.5h$ is indicative of the footprint of large-scales at the wall.

The low-rank maps for $c^+ = 18.9$ are shown in Fig. 3. Similar to the previous wave speed, there is good agreement between the energy spectrum from DNS and the low-rank map for resolvent analysis in Fig. 3(a). The agreement between the DNS and low-rank map for eddy analysis in Fig. 3(b), on the other hand, is worse than it was for the previous wave speed. The only area of slight agreement occurs for scales with the longest streamwise wavelengths from DNS. Perhaps the most remarkable aspect of the low-rank map in Fig. 3(b) is that it closely resembles the low-rank map in Fig. 2(b). The resolvent low-rank maps, on the other hand, are influenced significantly by the wave speed. It can be concluded that the wave speed does not have a significant impact on the eddy low-rank maps. For both wave speeds considered, there are two spanwise wavelengths for which the eddy operator is low-rank. The only difference is that \mathcal{R} for $c^+ = 18.9$ decreases for the smaller spanwise wavelength and increases for the larger spanwise wavelength relative to \mathcal{R} for $c^+ = 10$.

It can be remarked that the addition of eddy viscosity significantly distorts the linear mechanisms identified

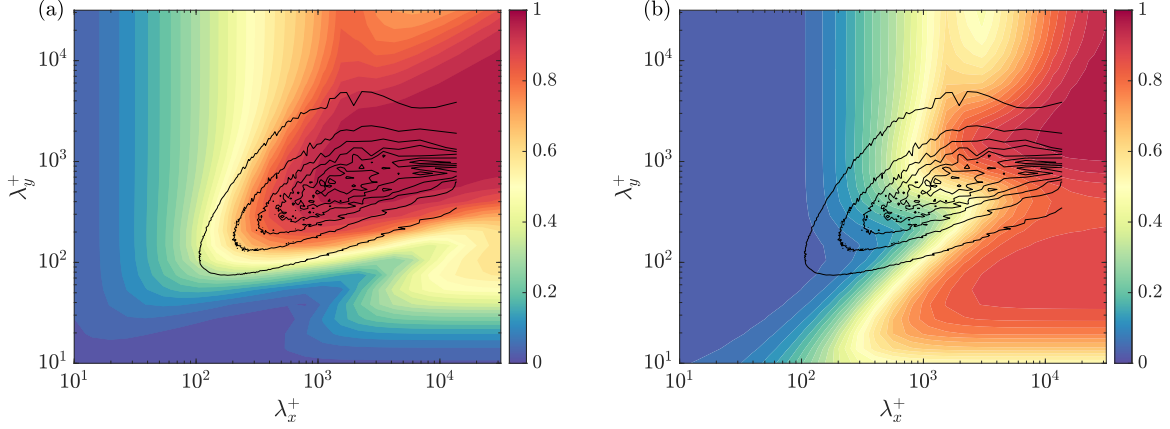


FIG. 3. Low-rank maps for (a) resolvent and (b) eddy analysis for a fixed wave speed of $c^+ = 18.9$. Contours of the turbulent kinetic energy spectrum at $z^+ = -h/2$ from Refs. [39] and [40] are denoted in black.

by resolvent analysis. As such, eddy analysis is less successful in identifying the energetic scales for a specified wave speed. These results, notwithstanding, do not quantify the accuracy of resolvent or eddy analysis in predicting flow structures in turbulent channel flow. It will be seen that the two peak spanwise wavelengths identified by the low-rank maps provide a valuable clue in identifying the types of structures that eddy analysis predicts with good accuracy.

B. Projection of resolvent modes onto SPOD modes

The objective of this section is to quantify the accuracy of resolvent and eddy analysis by projecting the leading SPOD mode $\hat{\mathbf{v}}_1(\mathbf{k})$ from DNS onto the leading resolvent $\hat{\boldsymbol{\psi}}_1(\mathbf{k})$ and eddy $\hat{\boldsymbol{\psi}}_1^e(\mathbf{k})$ modes. Similar analyses have been performed by Refs. [23] and [16] for turbulent pipe flow and turbulent jets, respectively. To account for the pairing of resolvent and eddy modes, the leading SPOD mode is projected onto both the first and second resolvent/eddy modes

$$\gamma(\mathbf{k}) = \sqrt{\left(\frac{\langle \hat{\mathbf{v}}_1(\mathbf{k}), \hat{\boldsymbol{\psi}}_1(\mathbf{k}) \rangle}{\|\hat{\mathbf{v}}_1(\mathbf{k})\| \cdot \|\hat{\boldsymbol{\psi}}_1(\mathbf{k})\|} \right)^2 + \left(\frac{\langle \hat{\mathbf{v}}_1(\mathbf{k}), \hat{\boldsymbol{\psi}}_2(\mathbf{k}) \rangle}{\|\hat{\mathbf{v}}_1(\mathbf{k})\| \cdot \|\hat{\boldsymbol{\psi}}_2(\mathbf{k})\|} \right)^2}, \quad (17a)$$

$$\gamma^e(\mathbf{k}) = \sqrt{\left(\frac{\langle \hat{\mathbf{v}}_1(\mathbf{k}), \hat{\boldsymbol{\psi}}_1^e(\mathbf{k}) \rangle}{\|\hat{\mathbf{v}}_1(\mathbf{k})\| \cdot \|\hat{\boldsymbol{\psi}}_1^e(\mathbf{k})\|} \right)^2 + \left(\frac{\langle \hat{\mathbf{v}}_1(\mathbf{k}), \hat{\boldsymbol{\psi}}_2^e(\mathbf{k}) \rangle}{\|\hat{\mathbf{v}}_1(\mathbf{k})\| \cdot \|\hat{\boldsymbol{\psi}}_2^e(\mathbf{k})\|} \right)^2}. \quad (17b)$$

Both projection coefficients $\gamma(\mathbf{k})$ and $\gamma^e(\mathbf{k})$ have a maximum value of unity, which indicates perfect alignment between SPOD and resolvent/eddy modes. A value of zero indicates that the mode shapes are orthogonal.

Figure 4 illustrates γ for wavenumbers that satisfy $1 \leq k_x \leq 19$ and $0 \leq k_y \leq 40$. These wavenumber pairs contain most of the kinetic energy in the flow and include structures associated with the near-wall cycle. Streamwise-constant modes are excluded since the wave speed is undefined for $k_x = 0$. They will be discussed in greater detail in Sec. V. The colorbar in Fig. 4 is restricted to a range of $[0.5, 1]$ to facilitate identification of wavenumber pairs where there is significant overlap between the SPOD and resolvent modes. Each panel in Fig. 4 represents a different wave speed. The lowest wave speed considered is $c^+ = 10.3$ in Fig. 4(a) and c^+ increases at increments of approximately 1.7, culminating in a wave speed of $c^+ = 18.9$ in Fig. 4(f). The lower bound on c^+ is motivated by the near-wall streaks being most energetic at a wall-normal location of $z^+ = 15$ where $U^+ \approx 10$ [1]. The upper bound on c^+ is chosen since it is approximately $c^+ = U_{CL}^+ - 2$, which translates to a wall-normal location of $z = -h/2$. Past studies [13, 15, 22] have noted good agreement

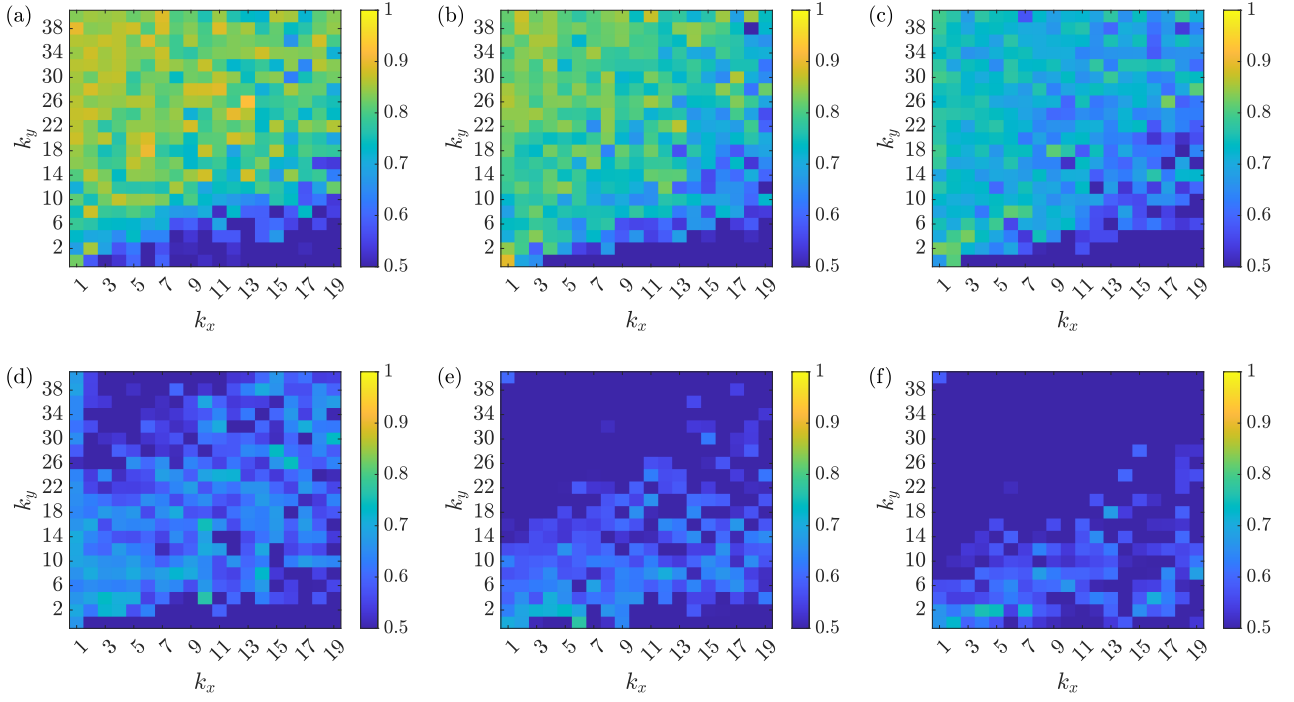


FIG. 4. Projection of the leading resolvent mode onto the leading SPOD mode for the wave speeds $c^+ = 10.3, 12.0, 13.7, 15.5, 17.2, 18.9$ in ascending order.

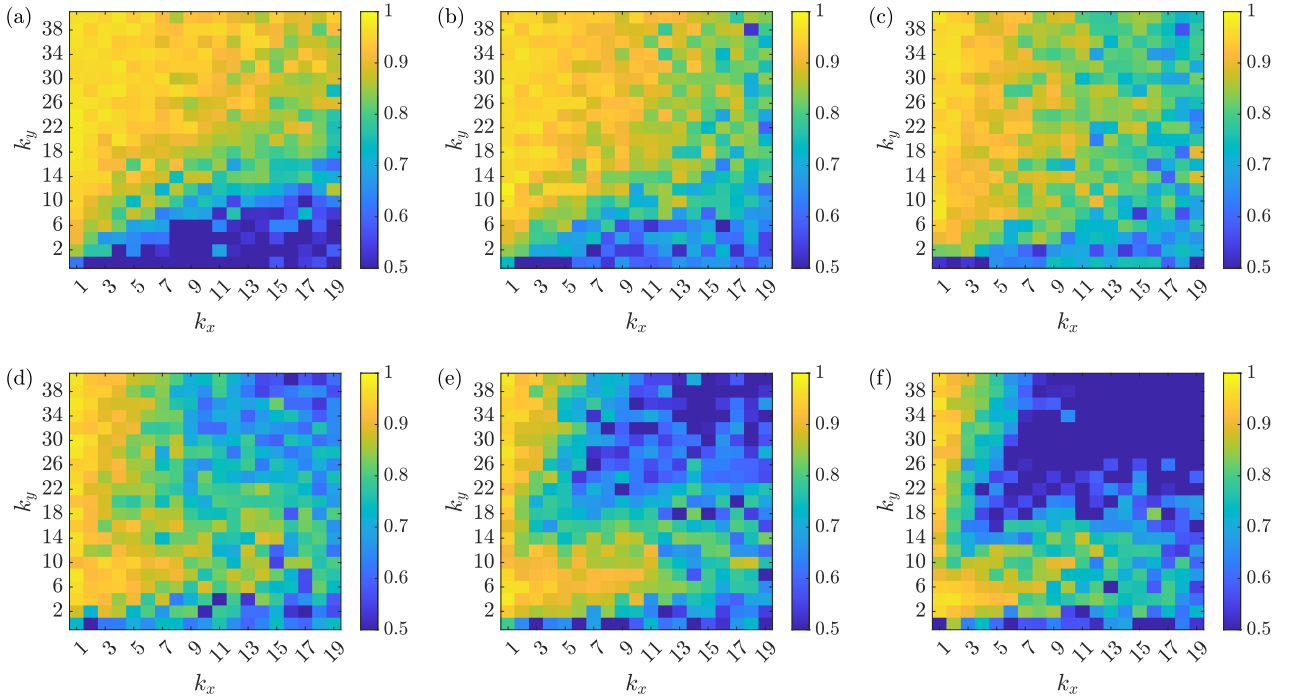


FIG. 5. Projection of the leading eddy mode onto the leading SPOD mode for the wave speeds $c^+ = 10.3, 12.0, 13.7, 15.5, 17.2, 18.9$ in ascending order.

between SPOD and eddy modes for structures that are most energetic at this wall-normal location. The eddy viscosity profile $\nu_T(z)$ also reaches a maximum at $z = -h/2$, an observation that is shown to be significant in Sec. V.

Figure 4 shows that there is good agreement between the leading SPOD and resolvent modes for $c^+ = 10.3$. Despite some outliers, Fig. 4(a) indicates that the highest projections are for modes that satisfy $k_x < k_y$. This is consistent with the results of Ref. [23] who noted that the lift-up mechanism leads to large amplification for high aspect ratio scales where $\mathcal{R} = k_y/k_x$. As the wave speed increases, however, the values of γ decline quite significantly, indicating poorer predictions of the mode shapes from resolvent analysis. Figure 5 presents the projection coefficient for eddy analysis. It is observed that there is significantly better agreement between the leading SPOD and eddy modes at all wave speeds in comparison to the standard resolvent in Fig. 4. There are, however, some similarities between γ and γ^e . First, the highest values of γ^e are obtained for high aspect ratio structures. Second, the wave speed has a major influence on γ^e . In general, the SPOD and eddy modes overlap less as the wave speed is increased. Unlike γ , however, there are several wavenumber pairs for which $\gamma^e > 0.9$ at the largest wave speed. The largest γ^e are clustered around the largest scales in Fig. 5(f) whereas in Fig. 5(a), they are centered around the near-wall cycle mode $(k_x, k_y) = (4, 30)$.

C. Frequency response

The previous sections show that there is a trade-off when eddy viscosity is added to the resolvent operator. On one hand, eddy viscosity distorts the linear dynamics of the operator such that the low-rank map resembles less the turbulent kinetic energy spectrum. On the other hand, the eddy modes have larger projections onto SPOD modes than their resolvent mode counterparts. Although these comparisons have been studied for a variety of wave speeds, the impact of eddy viscosity on the resolvent frequency response has yet to be analyzed. In order to be consistent with previous sections, the frequency response is considered from a wave speed point of view. The impact of eddy viscosity can be better appreciated by considering a single wavenumber pair initially before investigating all energetic wavenumber pairs as done in the previous sections. The wavenumber pair $(k_x, k_y) = (4, 30)$, which corresponds to $(\lambda_x^+, \lambda_y^+) = (864, 116)$, is selected as it corresponds to the near-wall streaks in the DNS used in this study.

To gain a better understanding of what the addition of eddy viscosity does to modify the frequency response of the resolvent operator, we look at a range of eddy viscosity based models, where the strength of the eddy viscosity is gradually increased from zero (equivalent to the standard resolvent) to the full eddy-viscosity. The strength of the eddy viscosity is adjusted artificially by introducing the scaling factor \mathcal{S} such that Eq. (10) becomes

$$\nu_T(z) = \frac{\nu}{2} \left(1 + \mathcal{S} \left[\frac{\kappa}{3} (1 - z^2)(1 + 2z^2)(1 - \exp(|z - 1|Re_\tau/A)) \right]^2 \right)^{1/2} + \frac{\nu}{2}, \quad (18)$$

where $\mathcal{S} \in [0, 1]$. Setting $\mathcal{S} = 0$ or $\mathcal{S} = 1$ is equivalent to resolvent analysis or eddy analysis, respectively. A similar parameter was introduced by Ref. [41] to derive a scale-dependent eddy viscosity for linear estimation of a turbulent channel flow at $Re_\tau = 2003$.

The first singular value σ_1 is plotted against c^+ in Fig. 6 for various strengths of eddy viscosity, i.e. different values of \mathcal{S} . As the value of \mathcal{S} increases, both the maximum amplification and the most amplified wave speed decrease. For this particular scale, moreover, the maximum amplification declines by a factor of 10 and the most amplified wave speed slows down substantially from $c^+ = 15.5$ to $c^+ = 9.5$. A crude explanation for this behavior is that the damping supplied by eddy viscosity results in slower, less amplified structures. Since resolvent analysis has absolutely no damping other than molecular viscosity, the structures are allowed to convect more quickly. It can, therefore, be expected that for an arbitrary scale the most amplified wave speed predicted by resolvent analysis is going to be greater than that predicted by eddy analysis.

This hypothesis is tested in Fig. 7, which compares the most energetic wave speed from DNS to the most amplified wave speed predicted by resolvent and eddy analysis. The only similarity among the three panels is that the most energetic/amplified wave speed is primarily governed by the spanwise wavenumber. Wider structures, i.e. those with small spanwise wavenumbers, travel faster than relatively less wide structures. The streamwise wavenumber plays a bigger role in DNS and resolvent analysis than it does for eddy analysis. Figures 7(a) and (b) show that for fixed k_y , the most energetic/amplified wave speed increases as a function

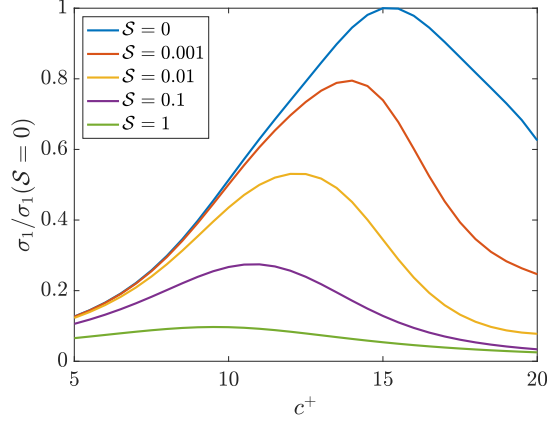


FIG. 6. Most energetic wave speed for $(k_x, k_y) = (4, 30)$ as a function of different strengths of the eddy viscosity as denoted by \mathcal{S} .

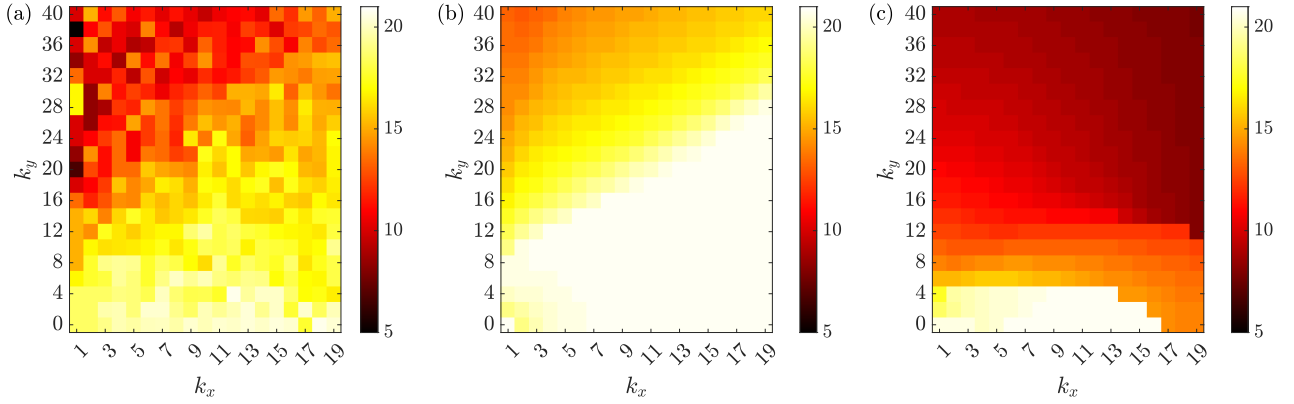


FIG. 7. Most energetic wave speed computed from (a) DNS compared to the most amplified wave speed predicted by (b) resolvent analysis and (c) eddy analysis.

of k_x . Thus, the trend for k_x is different from k_y in that longer structures, i.e. those with smaller k_x , travel slower, while wider structures, i.e. those with smaller k_y travel faster. Another interpretation of these trends is that higher aspect ratio structures convect more slowly and are thus more energetic closer to the wall. Lower aspect ratio structures, meanwhile, convect more quickly and are thus more energetic away from the wall. These trends are consistent with observations from Ref. [42] among others who report aspect ratios of approximately $\mathcal{R} = 8$ for near-wall coherent motions and $\mathcal{R} = 2 - 3$ for large-scale outer motions.

Figure 8 plots the difference between the most amplified wave speed predicted by resolvent/eddy analysis and the most energetic wave speed computed from DNS. Red squares indicate that the most amplified wave speed is too high and blue squares that the most amplified wave speed is too low. It is striking how large the differences are particularly for the relatively small Reynolds number considered in this study which restricts the range of wave speeds that can be expected in the flow. Figure 8(a) shows that the most amplified structures in resolvent analysis travel faster than their true speeds whereas in Fig. 8(b), the most amplified structures in eddy analysis travel slower. Despite the large differences between DNS and the linear analyses, there are two regions in Fig. 8(b) where the discrepancy is small. The first is denoted by the dashed, black rectangle and corresponds to small values of both k_x and k_y , where $c^+ \approx 18.9$. The second is denoted by the solid black rectangle, which contains wavenumber pairs in the range $(k_x, k_y) = (1 \leq k_x \leq 5, 30 \leq k_y \leq 34)$ where $c^+ \approx 10$. As will be discussed in the next section, the reasons for why these two wavenumber regions are estimated reasonably well by the eddy model can be related back to the wall-normal profile of the eddy viscosity $\nu_T(z)$.

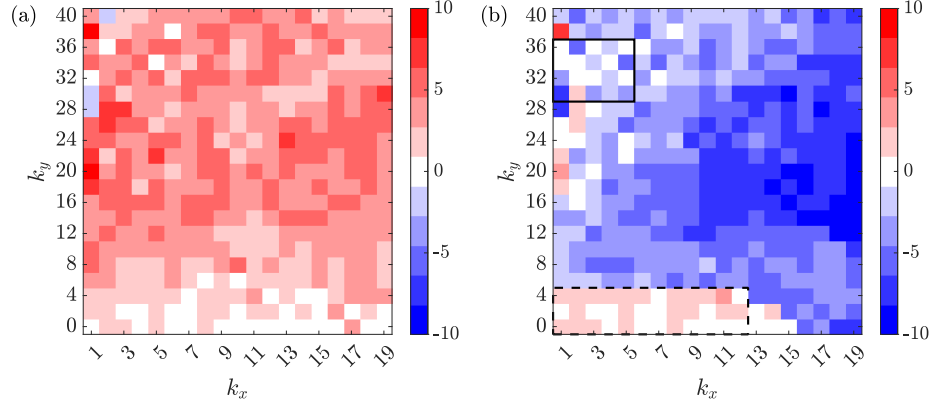


FIG. 8. Difference between the most amplified wave speed predicted by (a) resolvent and (b) eddy analysis compared to the most energetic wave speed computed in DNS.

Mode	k_x	k_y	$c_{\max, \text{SPOD}}^+$	$c_{\max, \text{resolvent}}^+$	$c_{\max, \text{eddy}}^+$	γ	γ^e	γ_{95}	γ_{95}^e
0	0	4	$\omega = 0$	$\omega = 0$	$\omega = 0$	0.898	0.978	6	2
1	1	2	18.5	19.0	18.5	0.663	0.956	36	2
2	2	8	16.8	20.5	13.8	0.586	0.907	56	8
3	4	30	10.1	15.3	9.50	0.864	0.959	40	2

TABLE II. The wavenumber triplets for modes 0-3 along with predictions from resolvent and eddy analysis.

V. MODE SHAPES AND THE CESS EDDY VISCOSITY PROFILE

The previous section analyzed the linear predictions of resolvent and eddy analysis using scalar quantities such as the low-rank maps, projection coefficients, and most amplified wave speeds. This section considers the wall-normal profiles of both mode shapes in Sec. V A and the Cess eddy viscosity profile itself in Sec. V B to predict the agreement between SPOD and resolvent/eddy modes at higher Reynolds numbers.

A. SPOD, resolvent, and eddy modes

The SPOD, resolvent, and eddy mode shapes are compared for four wavenumber triplets that are described in Table II. Mode 0 is a streamwise-constant mode and its most energetic frequency is $\omega = 0$. The other wavenumber pairs are chosen such that Modes 1, 2, and 3 have their peak energy around $z/h = -h/2$, $z/h = -h/4$, and $z^+ = 15$, respectively. The most energetic wave speed from SPOD is reported as $c_{\max, \text{SPOD}}^+$. Table II reports $c_{\max, \text{resolvent}}^+$ and $c_{\max, \text{eddy}}^+$, the most amplified wave speeds identified by resolvent and eddy analysis, respectively. The wave speed selected for plotting purposes, however, is kept fixed at $c_{\max, \text{SPOD}}^+$. The purpose of comparing $c_{\max, \text{SPOD}}^+$ and $c_{\max, \text{eddy}}^+$ is to emphasize that eddy analysis produces good predictions when $c_{\max, \text{SPOD}}^+ \approx c_{\max, \text{eddy}}^+$. The parameter $c_{\max, \text{resolvent}}^+$, meanwhile, does not provide information about the quality of predictions from resolvent analysis. Finally, Table II quantifies the number of resolvent/eddy modes needed such that the velocity from DNS is reconstructed to 95% accuracy. In other words, the number of modes required to obtain a value of $\gamma = 0.95$ using Eq. 17.

Figure 9 presents the SPOD, resolvent, and eddy mode for Mode 0. As indicated in Table II, both resolvent and eddy analysis correctly identify $\omega = 0$ as the most amplified frequency. The projection coefficients γ and γ^e are also large for this choice of \mathbf{k} . The number of resolvent or eddy modes needed to achieve $\gamma = 0.95$, therefore, is $\gamma_{95} = 6$ and $\gamma_{95}^e = 2$, respectively. The agreement between the resolvent and SPOD modes themselves, however, is not as compelling as $\gamma = 0.898$ might suggest. Although the streamwise velocity component is predicted reasonably well, the spanwise and wall-normal components are significantly underestimated due to the high non-normality of the resolvent operator [43, 44]. The eddy operator is also

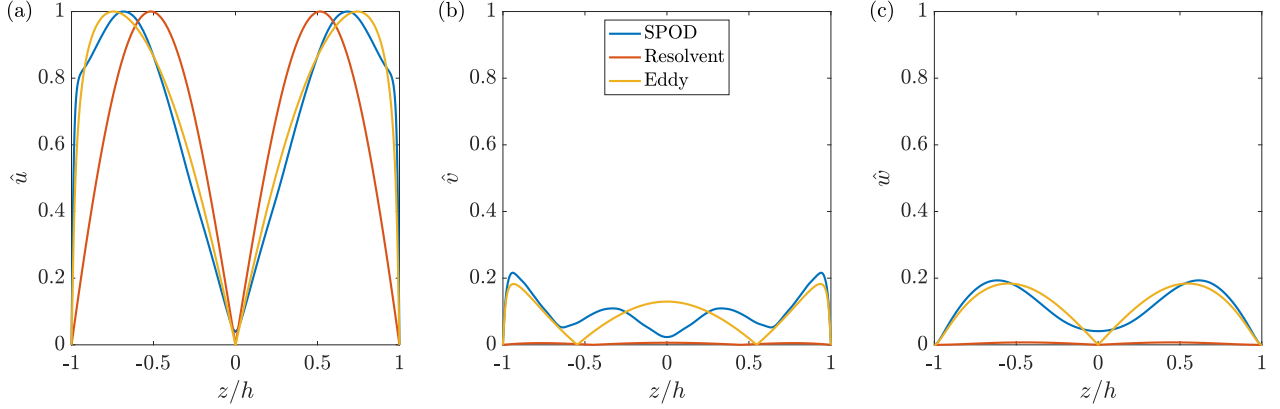


FIG. 9. The (a) streamwise, (b) spanwise, and (c) wall-normal component of the leading SPOD, resolvent, and eddy mode for Mode 0 for which $\mathbf{k} = (0, 4, \omega = 0)$.

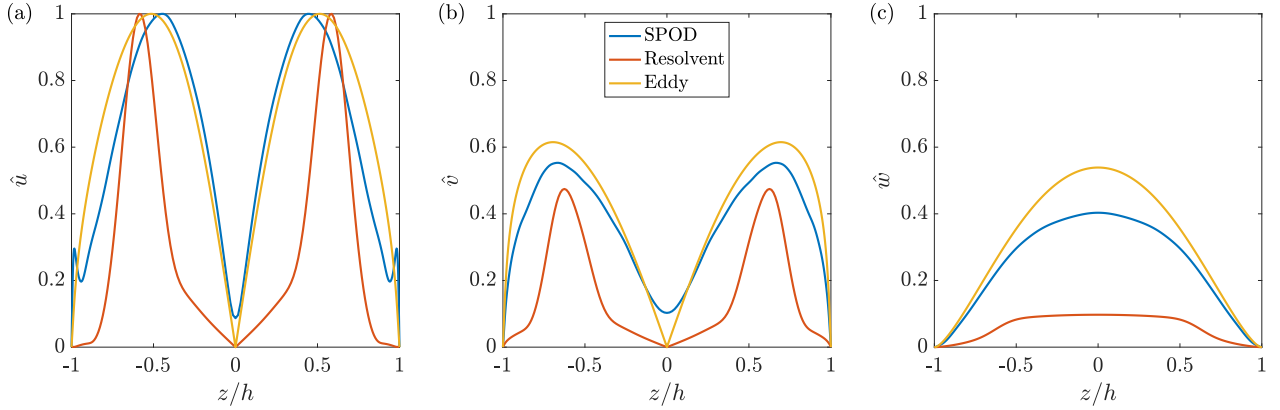


FIG. 10. The (a) streamwise, (b) spanwise, and (c) wall-normal component of the leading SPOD, resolvent, and eddy mode for Mode 1 for which $\mathbf{k} = (1, 2, 18.5)$.

non-normal but the addition of eddy viscosity results in a more normal operator [8]. Since the streamwise component is also dominant for the SPOD mode, it has a disproportionate influence on γ thus resulting in a higher value than might be expected from visual inspection of the mode shapes. The agreement between the SPOD and eddy modes, on the other hand, is good for all velocity components, resulting in $\gamma^e = 0.978$.

Mode 1 is an energetic structure in the outer region of the flow with a wavenumber triplet of $\mathbf{k} = (1, 2, 18.5)$. Table II shows that $c_{\max, \text{SPOD}}^+ = 18.5$ and this is in good agreement with predictions from resolvent and eddy analysis. Figure 10 illustrates that while the resolvent modes do not agree well with the SPOD modes, the eddy modes show reasonable agreement with SPOD. This is reflected in the projection coefficients as $\gamma^e = 0.956$ is higher than $\gamma = 0.663$. It also takes significantly fewer eddy modes to reconstruct the leading SPOD mode since as $\gamma_{95}^e = 2$ whereas $\gamma_{95} = 36$. Refs. [8, 13, 45] also observed that, when using resolvent modes, many suboptimal modes are needed to reconstruct the velocity field for high aspect ratio structures. One reason is that the streamwise and spanwise components of velocity are highly localized in the wall-normal direction due to the critical-layer mechanism [1, 13, 22, 46, 47]. The eddy modes, on the other hand, are smoothed out in z by the eddy viscosity. Another factor is that, similar to Mode 0, the wall-normal velocity component is underestimated by resolvent analysis as seen in Fig. 10(c). The agreement between the SPOD and eddy modes, meanwhile, is very good for all velocity components and wall-normal locations except the near-wall region of the streamwise component, as seen in Fig. 10(a).

Mode 2 is another structure in the outer region of the flow with a wavenumber triplet of $\mathbf{k} = (2, 8, 16.8)$. The streamwise velocity component is most energetic at $z/h = -0.75$ which is closer to the wall in comparison

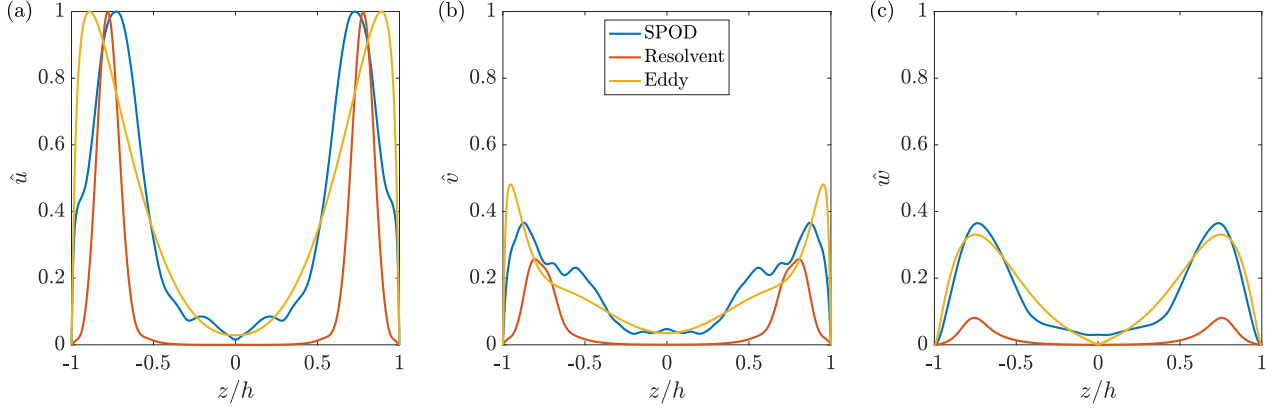


FIG. 11. The (a) streamwise, (b) spanwise, and (c) wall-normal component of the leading SPOD, resolvent, and eddy mode for Mode 2 for which $\mathbf{k} = (2, 8, 16.8)$.

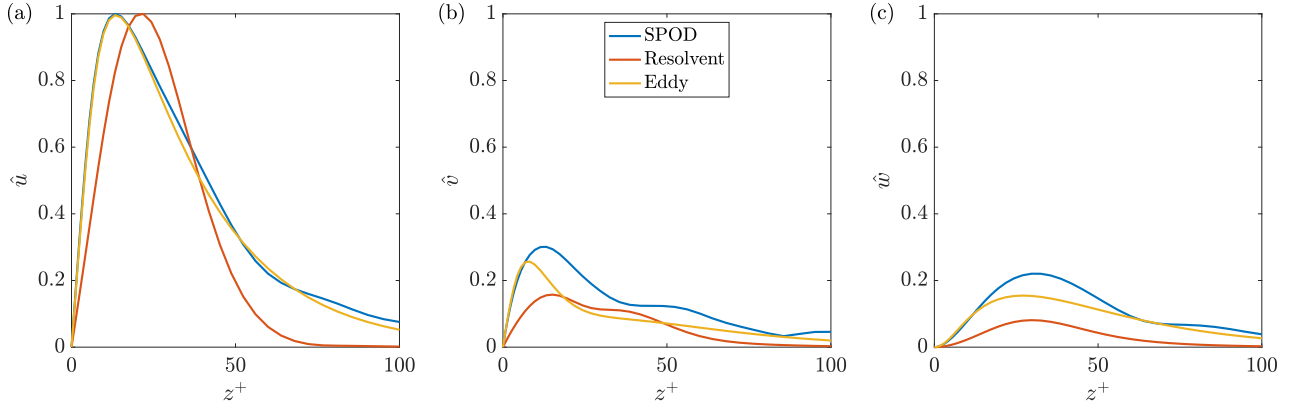


FIG. 12. The (a) streamwise, (b) spanwise, and (c) wall-normal component of the leading SPOD, resolvent, and eddy mode for Mode 3 for which $\mathbf{k} = (4, 30, 10.1)$.

to $z/h = -0.5$ for Mode 1. Neither resolvent nor eddy analysis are capable of predicting the most energetic wave speed for Mode 2. Consistent with the trends observed in Fig. 8, resolvent analysis predicts a wave speed that is too fast while eddy analysis predicts a wave speed that is too slow. As explained earlier, for plotting the resolvent and eddy modes in Fig. 11, $c_{resolvent}^+$ and c_{eddy}^+ are chosen to be the maximum wave-speed as identified by SPOD, i.e. $c_{max,SPOD}^+$. It can be remarked that the projection coefficients belie the true agreement between various mode shapes. When considering the resolvent modes, although $\gamma = 0.586$ seems low, the modes still capture the wall-normal location of the peak streamwise energy reasonably well. However, similar to Mode 1, the modes are localized about the critical-layer and the wall-normal component is underestimated resulting in a relatively low γ . The eddy modes appear to be in significantly better agreement as $\gamma^e = 0.907$. Unlike resolvent analysis, however, the wall-normal location of the peak in streamwise and spanwise energies of the eddy modes fall below their true locations, a trend that becomes more apparent for higher Reynolds numbers (see Ref. [22]). Even though it is not explicitly shown here for the sake of brevity, for structures with $c_{max,eddy}^+ < c_{max,SPOD}^+$, the peak streamwise and spanwise energies of the eddy mode are located below the correct wall-normal location identified by SPOD. Mode 2, consequently, is the only wavenumber triplet for which $\gamma_{95}^e = 8$ since suboptimal modes are required to “lift” the structure to its proper height. 58 modes, meanwhile, are required for resolvent modes to achieve $\gamma = 0.95$.

Figure 12 considers Mode 3, which is representative of the near-wall cycle. The agreement between the SPOD and resolvent wave speeds is poor but agreement between the mode shapes is high as $\gamma = 0.864$. Similar to Mode 0, the streamwise velocity component is the dominant component for Mode 3, thus relegating

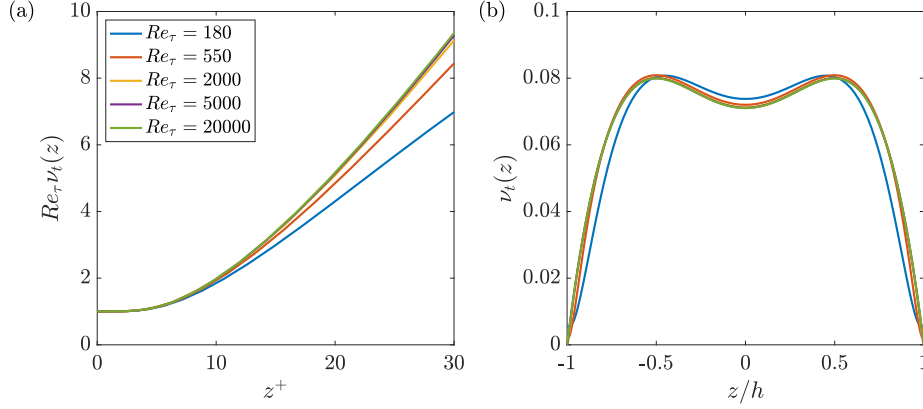


FIG. 13. Wall-normal profiles of (a) $Re_\tau \nu_t$ and (b) ν_t for various Re_τ .

the influence of the other two velocity components in computing γ . As seen in Table II, eddy analysis is close to identifying the most energetic wave speed. Furthermore, the SPOD and eddy mode shapes in Fig. 12, are in excellent agreement for the streamwise velocity component and good agreement for the spanwise and wall-normal velocity components, resulting in $\gamma^e = 0.959$. It is clear, furthermore, that eddy modes are a more efficient basis since $\gamma_{95}^e = 2$ compared to $\gamma_{95} = 40$. Similar agreement between DNS and eddy analysis predictions for near-wall structures has also been reported by Refs. [13, 15].

B. Cess eddy viscosity and effective Reynolds number

In this section, the Cess eddy viscosity profile is studied in greater detail in order to predict the agreement between SPOD and resolvent/eddy modes at higher Reynolds numbers. The profiles are obtained for a range of Reynolds numbers using Eq. (10). It is particularly interesting to look at the profiles around $z^+ = 15$ and $z = -h/2$ due to the good agreement between SPOD and eddy analysis for Modes 1 and 3 that have their peak energies at these wall-heights. In Fig. 13(a), the eddy viscosity profiles are pre-multiplied by Re_τ , resulting in a collapse near the wall. The profiles for $Re_\tau = 180$ and $Re_\tau = 550$ begin to diverge from the other Reynolds numbers around $z^+ = 10$ and $z^+ = 20$, respectively, but the agreement among all profiles is good, particularly around $z^+ = 15$. This wall-normal location is important since it coincides with the location of the structures associated with the near-wall cycle that travel at a wave speed of $c^+ = 10$. It therefore seems reasonable to assume that, for all Reynolds numbers, the eddy analysis will correctly predict the structures that are located at these wall-heights of $z^+ \approx 15$ and therefore convect at wave speeds around $c^+ = 10$. Consistent with this observation, Ref. [13] observed that at $Re_\tau = 1007$, the eddy analysis is able to get reasonable predictions for the structure $(k_x, k_y) = (14, 63)$ convecting at $c^+ = 10$.

In Fig. 13(b), $\nu_T(z)$ is plotted in outer units for Reynolds numbers in the range $180 \leq Re_\tau \leq 20000$. The profiles for all Reynolds numbers other than $Re_\tau = 180$ are virtually indistinguishable in the outer region. The largest differences occur near and at the walls where $\nu_T(0) = \nu_T(2h) = \nu$. The maximum value of ν_T is 0.08 and occurs at $z = \pm h/2$. Mode 1, for which the eddy analysis gives good predictions, was also found to be most energetic at this wall-height of $z = \pm h/2$. Since ν_T at $z = \pm h/2$ remains roughly constant with Reynolds number, it can be hypothesized that the eddy mode shapes for wavenumbers with $c_{\max}^+ = U^+(\pm h/2) \approx U_{CL}^+ - 2$ are unaffected by Re_τ . This hypothesis is tested in Fig. 14 where the mode shapes of structures with $c_{\max}^+ \approx U_{CL}^+ - 2$ are compared across different Re_τ . A second hypothesis, which is also tested in Fig. 14, is that the wall-normal-varying eddy viscosity $\nu_T(z)$ can be replaced by a constant eddy viscosity model, i.e. $\nu_T = Re_T$, where Re_T is the effective Reynolds number. For the case of a turbulent jet, References [14, 16, 48] showed that a constant eddy viscosity model can improve the agreement between SPOD and eddy modes.

Figure 14 compares the mode shapes for $\mathbf{k} = (1, 2, U_{CL}^+ - 2)$ from resolvent analysis, eddy analysis, and eddy analysis setting $Re_T = 1/(\max(\nu_T)) = 12.5$ as done in [49]. If $\nu_T = Re_T$, then only the mean profile is affected by changes in Reynolds number. All sets of modes are computed for the same Reynolds numbers

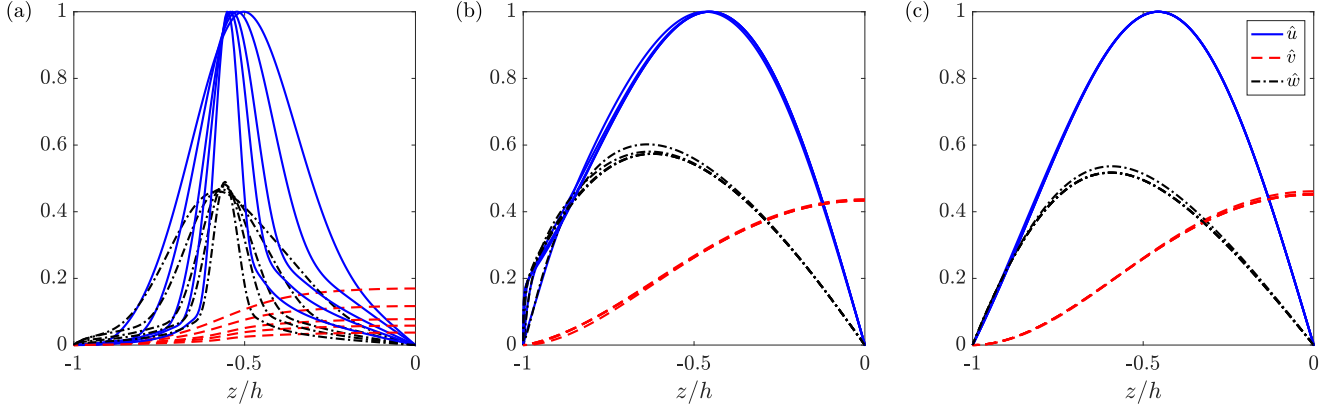


FIG. 14. Mode shapes for $\mathbf{k} = (1, 2, U_{CL}^+ - 2)$ from (a) resolvent analysis, (b) eddy analysis, and (c) eddy analysis setting $Re_T = 12.5$. The Reynolds numbers range from $Re_\tau = 180$ up to $Re_\tau = 20000$.

that appeared in Fig. 13 and are normalized by the maximum value of the streamwise velocity component. The resolvent modes in Fig. 14(a) are influenced heavily by the choice of Re_τ . The streamwise and spanwise velocity components become increasingly localized about the critical layer at $z = -h/2$ as the Reynolds number increases. The shape of the wall-normal component, on the other hand, is roughly constant but its magnitude relative to the wall-parallel velocity components decreases with increasing Reynolds number.

The impact of Reynolds number on the eddy and constant Re_T modes in Figs. 14(b,c) is negligible. The only difference among the eddy modes in Fig. 14(b) is that for $Re_\tau = 180$, the streamwise and spanwise velocity components are less attached to the wall in comparison to the other profiles which appear more blunt, i.e. flatter, near the wall. A similar difference emerges between the eddy and constant Re_T modes in that neither the streamwise nor spanwise components exhibit blunt behavior near the wall for any Reynolds number considered. The agreement between eddy and constant Re_T modes, nonetheless, is remarkable given that the constant eddy viscosity model is so simple.

The applicability of the constant eddy viscosity model, however, is limited to scales that have maximum streamwise energy at $z/h = \pm 0.5$. Figure 15 compares the mode shapes for $(k_x^+, k_y^+, c^+) = (2\pi/1000, 2\pi/100, 10)$, which are representative of the near-wall cycle, from resolvent analysis, eddy analysis, and eddy analysis setting $Re_T = 1/(\max(\nu_T)) = 12.5$. The Reynolds number has little impact on the resolvent and eddy modes but has a major impact on the constant Re_T modes. As the Reynolds number increases, the mode shapes become increasingly less localized about the critical layer. The location of the peak energy of all three velocity components, furthermore, gradually shifts closer to the channel centerline and away from the wall. Although it is not shown in the interest of brevity, the same trends can be observed for other values of Re_T . The wall-varying profile of the eddy viscosity near the wall, consequently, is essential to capture the correct mode shapes for wavenumber triplets that are associated with the near-wall cycle.

VI. NONLINEAR ENERGY TRANSFER AND EDDY VISCOSITY

The improved agreement between SPOD and eddy modes indicates that eddy viscosity is able to partially model the effect of $\hat{\mathbf{f}}$ for particular scales such as Modes 1 and 3. In this section, the energy transfers that are introduced by the eddy viscosity, herein referred to as eddy dissipation, are examined in greater detail to explain the success or failure of eddy analysis in predicting the correct structures. Section VIA introduces eddy dissipation which consists of two terms. The first originates from the wall-normal-varying effective Reynolds number $\nu_T(z) - \nu$ and the second from the eddy viscosity gradient $\nu_T' = d\nu_T/dz$. In Sec. VIB, the wall-normal profiles of these two transfers are examined in order to determine how they affect the eddy mode shapes. It is demonstrated in Sec. VIC that artificially adjusting the eddy viscosity gradient can significantly manipulate the eddy mode shapes, particularly in the near-wall region. Section VID discusses the types of interactions that are modelled by the eddy viscosity.

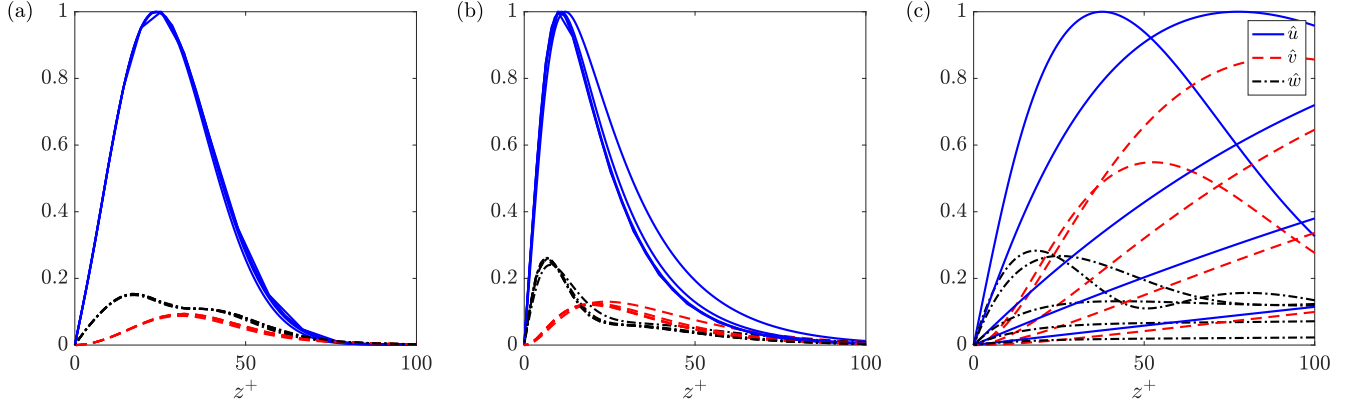


FIG. 15. Mode shapes for $(k_x^+, k_y^+, c^+) = (2\pi/1000, 2\pi/100, 10)$ from (a) resolvent analysis, (b) eddy analysis, and (c) eddy analysis setting $Re_T = 12.5$. The Reynolds numbers range from $Re_\tau = 180$ up to $Re_\tau = 20000$.

A. Eddy Dissipation

As explained in Ref. [8], the addition of eddy viscosity introduces new dissipation terms into the kinetic energy balance for each scale. These terms can be derived by expanding the viscous term in Eq. (9) and Fourier-transforming in the homogeneous directions

$$\nabla \cdot [\nu_T (\nabla \hat{\mathbf{u}} + \nabla \hat{\mathbf{u}}^T)] = \nu_T \nabla^2 \hat{\mathbf{u}} + (\nabla \cdot \nu_T) (\nabla \hat{\mathbf{u}} + \nabla \hat{\mathbf{u}}^T). \quad (19)$$

Rewriting Eq. (19) in index notation, taking the inner product with respect to u_i , and averaging the final expression in time yields

$$\hat{\mathcal{D}}_T(k_x, k_y, z) = \underbrace{-\nu \overline{\frac{\partial \hat{u}_i}{\partial x_j} \frac{\partial \hat{u}_i}{\partial x_j}}}_{\hat{\mathcal{D}}(k_x, k_y, z)} - \underbrace{(\nu_T(z) - \nu) \overline{\frac{\partial \hat{u}_i}{\partial x_j} \frac{\partial \hat{u}_i}{\partial x_j}}}_{\hat{\mathcal{V}}(k_x, k_y, z)} + \underbrace{\frac{d\nu_T(z)}{dz} \hat{u}_i \left(\frac{\partial \hat{u}_i}{\partial z} + \frac{\partial \hat{w}}{\partial x_i} \right)}_{\hat{\mathcal{G}}(k_x, k_y, z)}, \quad (20)$$

where $i, j = 1, 2, 3$ and $\hat{\mathcal{D}}_T$ is dissipation due to molecular and eddy viscosity. $\hat{\mathcal{D}}_T$ can be split into three separate terms: $\hat{\mathcal{D}}$ is dissipation due to molecular viscosity, $\hat{\mathcal{V}}$ is additional dissipation introduced by a wall-varying effective Reynolds number $\nu_T(z) - \nu$, and $\hat{\mathcal{G}}$ is dissipation due to the wall-normal gradient of the eddy viscosity profile. The combined effect of $\hat{\mathcal{V}} + \hat{\mathcal{G}}$ can be referred to as eddy dissipation, i.e. $\widehat{Edd} = \hat{\mathcal{V}} + \hat{\mathcal{G}}$. It can be noted that without eddy viscosity, $\widehat{Edd} = \hat{\mathcal{V}} = \hat{\mathcal{G}} = 0$.

B. Positive and negative energy transfers

It is guaranteed that $\hat{\mathcal{D}}$ and $\hat{\mathcal{V}}$ are real and negative at all wall-normal locations, but this is not the case for $\hat{\mathcal{G}}$. In fact, it can be shown that $\hat{\mathcal{G}}$ is likely to be positive near the wall. If the final term of Eq. (20) is expanded in full, then $\hat{\mathcal{G}}$ becomes

$$\hat{\mathcal{G}} = \frac{d\nu_T}{dz} \hat{u} \overline{\frac{\partial \hat{u}}{\partial z}} + \frac{d\nu_T}{dz} \hat{v} \overline{\frac{\partial \hat{v}}{\partial z}} + 2 \frac{d\nu_T}{dz} \hat{w} \overline{\frac{\partial \hat{w}}{\partial z}} + \frac{d\nu_T}{dz} \hat{u} \overline{\frac{\partial \hat{w}}{\partial x}} + \frac{d\nu_T}{dz} \hat{v} \overline{\frac{\partial \hat{w}}{\partial y}}. \quad (21)$$

Assuming that the streamwise velocity component is significantly stronger than the spanwise and wall-normal components, i.e. $\hat{u} \gg \hat{v}, \hat{w}$, and that wall-normal gradients dominate over streamwise and spanwise gradients, Eq. (21) can be approximated as

$$\hat{\mathcal{G}} \approx \frac{d\nu_T}{dz} \hat{u} \overline{\frac{\partial \hat{u}}{\partial z}}. \quad (22)$$

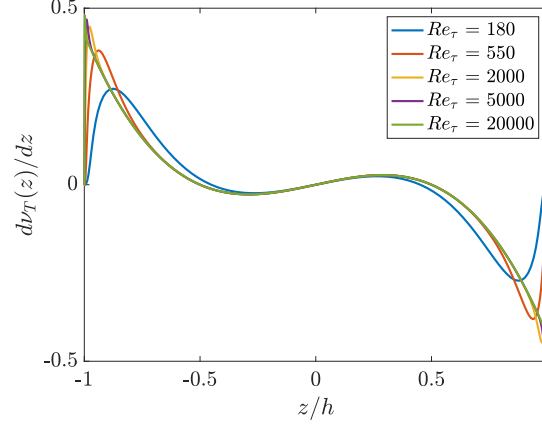


FIG. 16. Wall-normal profiles of the eddy viscosity gradient ν_T' for various Re_τ

For the lower wall, $\hat{u} = 0$ due to the no-slip condition and both \hat{u} and $\frac{\partial \hat{u}}{\partial z}$ must be either both positive or negative moving away from the wall. In either case, the product of \hat{u} and $\frac{\partial \hat{u}}{\partial z}$ is positive. As shown in Fig. 16, $\frac{d\nu_T}{dz} > 0$ near the lower wall so the product of all three terms that appear in Eq. 22 is positive in the near-wall region. Although several approximations have been made to arrive at this result, it is significant because \hat{V} and \hat{G} attempt to model nonlinear transfer processes. If \hat{G} can be positive at a given wall-normal location, then it implies that eddy viscosity can model locally both positive and negative energy transfer. The net energy transfer due to eddy viscosity that is obtained by integrating \widehat{Edd} over the wall-normal direction tends to be negative [8].

Before examining profiles of $\hat{V}(z)$ and $\hat{G}(z)$ for specific scales, it is worth commenting further on the eddy viscosity gradient profiles in Fig. 16. Similar to the ν_T profiles in Fig. 13, it can be observed that Re_τ has a negligible impact on ν_T' for most wall-normal locations. The maxima and minima of profiles become more extreme and closer to the wall as Re_τ increases. This localization suggests that $\hat{G}(z)$ is likely to be more concentrated in the near-wall regions and have a larger magnitude for higher Reynolds numbers.

Figure 17(a) compares $\hat{Q}(z) = -\hat{u}_i \frac{\partial}{\partial x_j} \widehat{u_i u_j}$, the time-averaged nonlinear transfer from DNS, for $(k_x, k_y) = (0, 4)$ with $\widehat{Edd}(z)$ in Fig. 17(b). Since the DNS results are averaged in time, they include contributions from all frequencies (wave speeds) whereas the eddy predictions are for the most energetic frequency only. This is a reasonable approximation since $\omega = 0$ dominates over all other frequencies (recall that wave speed is ill-defined for $k_x = 0$ modes). There is good agreement between $\hat{Q}(z)$ and $\widehat{Edd}(z)$ at nearly all wall-normal locations other than the near-wall region. Eddy dissipation correctly predicts positive energy transfer near the wall but its magnitude is too large. In Fig. 17(c), $\widehat{Edd}(z)$ is split into the contributions from $\hat{V}(z)$ and $\hat{G}(z)$. Fig. 17(c) reinforces that $\hat{G}(z)$ is responsible for the positive energy transfer, as predicted by Eq. (22), and that $\hat{V}(z)$ accounts for the bulk of the negative energy transfer.

Figure 18(a) compares $\hat{Q}(z)$ for $(k_x, k_y) = (4, 30)$ with $\widehat{Edd}(z)$ in Fig. 18(b). The eddy predictions are for the most energetic wave speed $c^+ = 10$. Good agreement can be observed between $\hat{Q}(z)$ and $\widehat{Edd}(z)$ although the eddy dissipation is most negative at $z^+ = 20$ instead of $z^+ = 15$. Similar to the previous scale, eddy dissipation overestimates the positive energy transfer in the near-wall region which, as seen in Fig. 18(c), is driven by $\hat{G}(z)$. The contribution from $\hat{V}(z)$, on the other hand, is negative at all wall-normal locations. It can be concluded that the eddy viscosity gradient plays an important role in modeling positive energy transfer processes. The predicted $\widehat{Edd}(z)$, nonetheless, exceeds the true nonlinear transfer in the near-wall region. The next section considers the effect of artificially weakening the eddy viscosity gradient to analyze its impact on the resulting mode shapes.

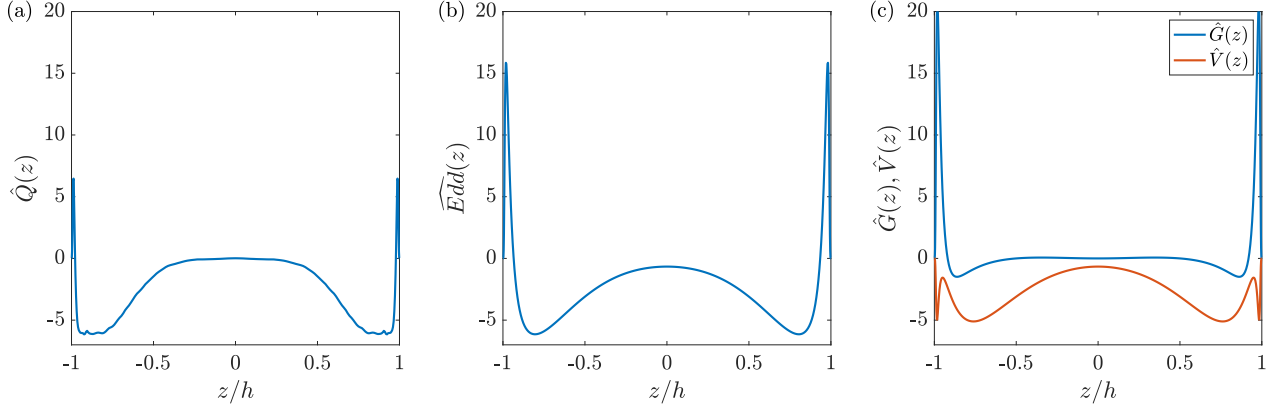


FIG. 17. (a) Time-averaged nonlinear transfer from DNS for $(k_x, k_y) = (0, 4)$ compared to (b) eddy dissipation and (c) its components for $\omega = 0$.

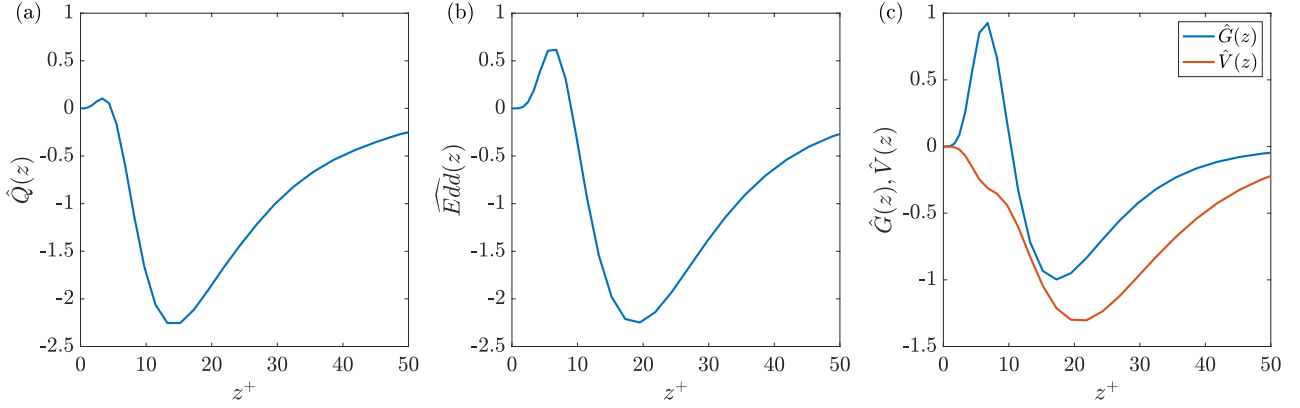


FIG. 18. (a) Time-averaged nonlinear transfer from DNS for $(k_x, k_y) = (4, 30)$ compared to (b) eddy dissipation and (c) its components for $c^+ = 10$.

C. Artificially adjusting the eddy viscosity gradient

In this section, the strength of the eddy viscosity term is altered by introducing a scaling factor \mathcal{G} such that Eq. (19) becomes

$$\nabla \cdot [\nu_T(\nabla \hat{\mathbf{u}} + \nabla \hat{\mathbf{u}}^T)] = \nu_T \nabla^2 \hat{\mathbf{u}} + \mathcal{G}(\nabla \cdot \nu_T)(\nabla \hat{\mathbf{u}} + \nabla \hat{\mathbf{u}}^T), \quad (23)$$

where $\mathcal{G} \geq 0$ controls the strength of the eddy viscosity gradient term. Figure 19 illustrates the impact of artificially adjusting \mathcal{G} for Mode 0. It can be seen that as \mathcal{G} increases, the peak energy of the streamwise and spanwise velocity components shifts closer to the wall. The shape of the wall-normal velocity component is less affected but its magnitude decreases. It can be reasoned that increasing \mathcal{G} results in greater positive energy transfer in the near-wall region. The energy of the modes, consequently, is redistributed towards the wall and to the wall-parallel velocity components. For some scales, \mathcal{G} is too strong, resulting in too much energy in the streamwise and spanwise velocity components near the wall as seen for Mode 2 in Sec. V A. These biased mode shapes explain why linear-based estimation techniques that use an eddy viscosity model, e.g. Refs. [41, 46], overpredict the strength of fluctuations in the near-wall region when measurements are known in the logarithmic region. The biased mode shapes are also consistent with Ref. [21] who found that the eddy viscosity model underestimates fluctuations when using wall-based measurements.

Figure 20 presents the effect of \mathcal{G} on the Mode 1 shapes. Unlike Mode 0, \mathcal{G} has almost no impact on the structures although the spanwise component becomes slightly less energetic relative to the other velocity

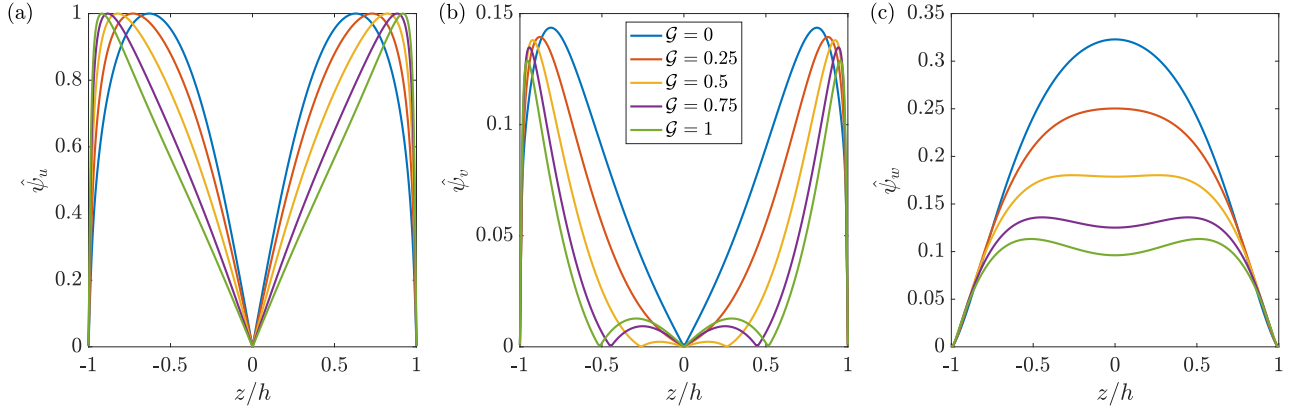


FIG. 19. Leading eddy modes for $\mathbf{k} = (0, 4, 0)$ for various strengths of the eddy viscosity gradient \mathcal{G} .

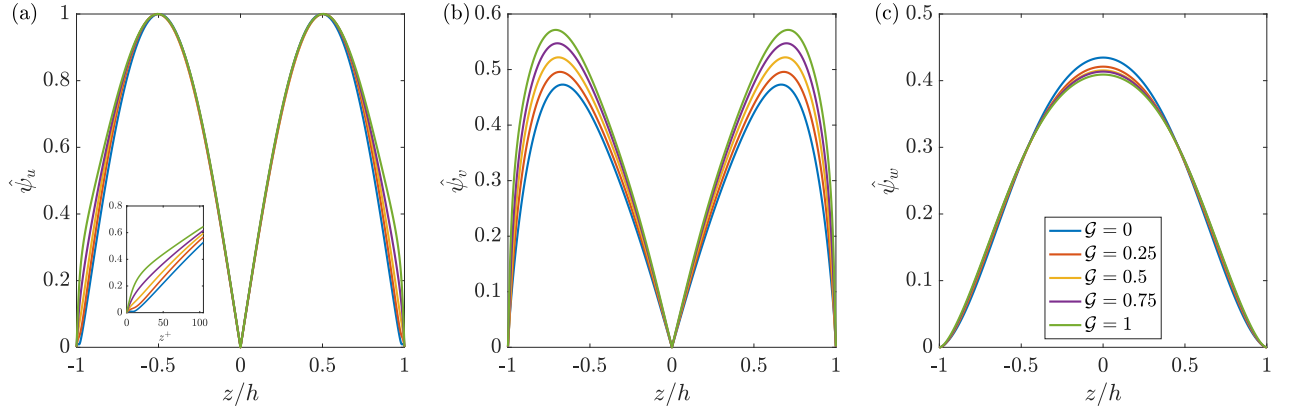


FIG. 20. Leading eddy modes for $\mathbf{k} = (1, 2, 18.5)$ for various strengths of the eddy viscosity gradient \mathcal{G} .

components as \mathcal{G} increases. The main difference occurs in the streamwise velocity component very close to the wall. The inset of Fig. 19 shows that the mode shape becomes flatter or more blunt as \mathcal{G} increases. Similar to Mode 0, the flatter profiles can be attributed to \hat{G} injecting energy in this region of the flow. This also explains why the constant eddy viscosity model, which has a wall-normal gradient of zero everywhere, was not able to reproduce the near-wall behavior in Fig. 14(c) that appeared in Fig. 14(b).

D. Discussion

The previous sections have analyzed the energy transfer processes that can be modeled by the Cess eddy viscosity profile. This section aims to contextualize these results with respect to recent low-order modeling efforts in the literature. One key challenge is to identify the smallest subset of nonlinear interactions that are needed to sustain a wall-bounded turbulent flow at high Reynolds numbers. The generalized quasi-linear (GQL) approximation [50], in particular, is able to reproduce key statistical features of wall-bounded turbulence [30]. The GQL approximation decomposes the flow into a low-wavenumber group and a high-wavenumber group. Nonlinear interactions involving the high-wavenumber group are removed. If the low-wavenumber group is restricted to the mean flow, the quasi-linear approximation (QLA) is recovered [51–54].

Reference [30] has shown that the GQL approach retains triadic interactions that are responsible for the scattering mechanism and inverse energy transfer in the near-wall region. The former can be attributed to low-high wavenumber interactions that feed into high wavenumbers while the latter arise from high-high wavenumber interactions that feed into low wavenumbers. It is posited that the negative energy transfer

modeled by eddy viscosity through \hat{V} can be interpreted as a scattering mechanism that removes energy from larger scales and redistributes it to smaller scales. The positive energy transfer modeled by \hat{G} , on the other hand, reproduces the inverse energy transfer in the near-wall region. The combined effect of these two transfers, therefore, encapsulates the effect of small scales on the large scales.

VII. CONCLUSIONS

The predictions of resolvent analysis with and without eddy viscosity have been evaluated for a friction Reynolds number of $Re_\tau = 550$. The accuracy of the predictions were assessed using scalar measures including low-rank maps of the operator, projection coefficients, and the most amplified wave speed as well as direct comparison of the structures. The addition of eddy viscosity distorted the linear amplification mechanisms that are identified by resolvent analysis. As such, the low-rank maps of the eddy operator did not align well with the turbulent kinetic energy spectrum in comparison to the low-rank maps of the standard resolvent operator. For eddy analysis, low-rank behavior was identified for structures with spanwise wavelengths of $\lambda_y^+ \approx 80$ and $\lambda_y/h = 3.5$ independent of the wave speed under investigation. This is consistent with previous transient growth and optimal harmonic forcing studies [12, 35].

Despite the distorted low-rank maps, the predictions from eddy analysis were generally in better agreement with DNS in comparison to resolvent analysis. The highest projection coefficients were obtained for eddy modes with wave speeds of $c^+ = 10$ and $c^+ = 18.9$. These correspond to structures associated with the near-wall cycle and structures that are most energetic at $z/h = \pm 0.5$. The most amplified wave speed identified by eddy analysis was also found to match the most energetic wave speed in DNS for these two types of structures. For most wavenumber pairs, however, both resolvent and eddy analysis failed to predict the most energetic wave speed. Resolvent analysis overestimated the correct wave speed while eddy analysis underestimated the correct wave speed.

The importance of wave speed on the projection coefficients motivated the selection of specific scales for comparing the SPOD modes to the resolvent and eddy modes. Consistent with previous studies, resolvent modes tended to be localized around the critical layer [1] and the streamwise velocity component was too strong relative to the spanwise and wall-normal velocity components. All three velocity components of the eddy modes, meanwhile, matched their SPOD counterparts for the wave speeds of $c^+ = 10$ and $c^+ = 18.9$. For other wave speeds, eddy analysis mostly underestimated the most energetic wave speed and predicted structures that were energetic closer to the wall than the SPOD modes. It was concluded that for higher Reynolds numbers, SPOD and eddy modes will agree for $c^+ = 10$ and $c^+ = U_{CL}^+ - 2$ due to the invariance of the Cess profile in the near-wall region up to $z^+ = 15$, when it is premultiplied by Re_τ , and in the outer region where it is maximum at $z/h = \pm 0.5$. Modes for $c^+ = U_{CL}^+ - 2$ could also be obtained with reasonable accuracy from eddy analysis by setting constant $\nu_T = Re_T = 12.5$.

Finally, there was an investigation into the energy processes that are modeled by the Cess profile. Two transfers were identified, one of which is an effective Reynolds number that varies spatially. Similar to dissipation, the effective Reynolds number term is guaranteed to be real and negative. The second term originates from the eddy viscosity gradient, which tends to be positive in the near-wall region. The combined effect, called eddy dissipation, models well the actual nonlinear transfer taking place in DNS although the positive energy transfer near the wall is overestimated. This explains the tendency for eddy modes to be too energetic near the wall as observed for higher Reynolds numbers in Ref. [22] and in linear-based estimation, e.g. Ref. [46].

In order to further improve predictions from resolvent analysis, the Cess profile could be replaced with a scale-dependent eddy viscosity. Reference [16], for example, solved an inverse problem to find the eddy viscosity profile that maximized the projection of the leading resolvent mode onto the leading SPOD mode. The drawback of this approach is that it requires sufficient data in order to compute the leading SPOD mode. As such, other approaches have modified the Cess profile using scaling arguments [41] or a stochastic approach to model background turbulence that can inject or dissipate energy of coherent waves [26]. Regardless of the approach selected, the Cess profile provides a good initial condition for optimizing an eddy viscosity or modeling the effect of nonlinear terms as done in Ref. [55].

ACKNOWLEDGMENTS

The authors would like to acknowledge the use of the IRIDIS High Performance Computing Facility, and associated support services at the University of Southampton.

Appendix A: Linear operators

After elimination of the pressure, the linearized Navier-Stokes equations can be rewritten for the wall-normal velocity \hat{w} and wall-normal vorticity $\hat{\eta} = ik_y \hat{u} - ik_x \hat{v}$. The matrices \mathbf{A} , \mathbf{B} , and \mathbf{C} that appear in (4) are

$$\mathbf{A} = \mathbf{M} \begin{bmatrix} \mathcal{L}_{OS} & 0 \\ -ik_y U' & \mathcal{L}_{SQ} \end{bmatrix}, \quad (\text{A1a})$$

$$\mathbf{B} = \mathbf{M} \begin{bmatrix} -ik_x \mathcal{D} & -ik_y \mathcal{D} & -k^2 \\ ik_y & -ik_x & 0 \end{bmatrix}, \quad (\text{A1b})$$

$$\mathbf{C} = \frac{1}{k^2} \begin{bmatrix} ik_x \mathcal{D} & -ik_y \\ ik_y \mathcal{D} & ik_x \\ k^2 & 0 \end{bmatrix}. \quad (\text{A1c})$$

Both \mathcal{D} and $'$ represent differentiation in the wall-normal direction and $k^2 = k_x^2 + k_y^2$. The mass matrix \mathbf{M} is defined as

$$\mathbf{M}(k_x, k_y) = \begin{bmatrix} \Delta^{-1} & 0 \\ 0 & \mathbf{I} \end{bmatrix}, \quad (\text{A2})$$

where $\Delta = \mathcal{D}^2 - k^2$ and \mathbf{I} is the identity matrix. The Orr-Sommerfeld \mathcal{L}_{OS} and Squire \mathcal{L}_{SQ} operators are

$$\mathcal{L}_{OS} = -ik_x U \Delta + ik_x U'' + (1/Re_\tau) \Delta^2, \quad (\text{A3a})$$

$$\mathcal{L}_{SQ} = -ik_x U + (1/Re_\tau) \Delta. \quad (\text{A3b})$$

With the addition of eddy viscosity, they become

$$\mathcal{L}_{OS} = -ik_x U \Delta + ik_x U'' + \nu_T \Delta^2 + 2\nu_T' \mathcal{D} \Delta + \nu_T'' (\mathcal{D}^2 + k^2), \quad (\text{A4a})$$

$$\mathcal{L}_{SQ} = -ik_x U + \nu_T \Delta + \nu_T' \mathcal{D}. \quad (\text{A4b})$$

-
- [1] B. J. McKeon and A. S. Sharma, “A critical layer framework for turbulent pipe flow,” *J. Fluid Mech.* **658**, 336–382 (2010).
 - [2] A. S. Sharma, R. Moarref, B. J. McKeon, J. S. Park, M. D. Graham, and A. P. Willis, “Low-dimensional representations of exact coherent states of the Navier-Stokes equations from the resolvent model of wall turbulence,” *Phys. Rev. E* **93**, 021102 (2016).
 - [3] R. Moarref, A. S. Sharma, J. A. Tropp, and B. J. McKeon, “Model-based scaling of the streamwise energy density in high-Reynolds-number turbulent channels,” *J. Fluid Mech.* **734**, 275–316 (2013).
 - [4] N. Skouloudis and Y. Hwang, “Scaling of turbulence intensities up to $Re_\tau = 10^6$ with a resolvent-based quasilinear approximation,” *Phys. Rev. Fluids* **6**, 034602 (2021).
 - [5] M. Luhar, A. S. Sharma, and B. J. McKeon, “Opposition control within the resolvent analysis framework,” *J. Fluid Mech.* **749**, 597–626 (2014).

- [6] S. Nakashima, K. Fukagata, and M. Luhar, “Assessment of suboptimal control for turbulent skin friction reduction via resolvent analysis,” *J. Fluid Mech.* **828**, 496–526 (2017).
- [7] S. S. Toedtli, M. Luhar, and B. J. McKeon, “Predicting the response of turbulent channel flow to varying-phase opposition control: Resolvent analysis as a tool for flow control design,” *Phys. Rev. Fluids* **4**, 073905 (2019).
- [8] S. Symon, S. J. Illingworth, and I. Marusic, “Energy transfer in turbulent channel flows and implications for resolvent modelling,” *J. Fluid Mech.* **911**, A3 (2021).
- [9] B. Jin, S. Symon, and S. J. Illingworth, “Energy transfer mechanisms and resolvent analysis in the cylinder wake,” *Phys. Rev. Fluids* **6**, 024702 (2021).
- [10] W. C. Reynolds and A. K. M. F. Hussain, “The mechanics of an organized wave in turbulent shear flow. Part 3. Theoretical models and comparisons with experiments,” *J. Fluid Mech.* **54**, 263–288 (1972).
- [11] G. Pujals, M. García-Villalba, C. Cossu, and S. Depardon, “A note on optimal transient growth in turbulent channel flows,” *Phys. Fluids* **21**, 015109 (2009).
- [12] Y. Hwang and C. Cossu, “Linear non-normal energy amplification of harmonic and stochastic forcing in the turbulent channel flow,” *J. Fluid Mech.* **664**, 51–73 (2010).
- [13] P. Morra, O. Semeraro, D. S. Henningson, and C. Cossu, “On the relevance of Reynolds stresses in resolvent analysis of turbulent wall-bounded flows,” *J. Fluid Mech.* **867**, 969–984 (2019).
- [14] P. Kuhn, J. Soria, and K. Oberleithner, “Linear modelling of self-similar jet turbulence,” *J. Fluid Mech.* **919**, A7 (2021).
- [15] P. Morra, P. A. S. Nogueira, A. V. G. Cavalieri, and D. S. Henningson, “The colour of forcing statistics in resolvent analyses of turbulent channel flows,” *J. Fluid Mech.* **907**, A24 (2021).
- [16] E. Pickering, G. Rigas, O. T. Schmidt, D. Sipp, and T. Colonius, “Optimal eddy viscosity for resolvent-based models of coherent structures in turbulent jets,” *J. Fluid Mech.* **917**, A29 (2021).
- [17] J. L. Lumley, *Stochastic tools in turbulence* (Academic Press, 1967).
- [18] C. Picard and J. Delville, “Pressure velocity coupling in a subsonic round jet,” *Int. J. Heat Fluid Flow* **21**, 359–364 (2000).
- [19] A. Towne, O. T. Schmidt, and T. Colonius, “Spectral proper orthogonal decomposition and its relationship to dynamic mode decomposition and resolvent analysis,” *J. Fluid Mech.* **847**, 821–867 (2018).
- [20] P. A. S. Nogueira, P. Morra, E. Martini, A. V. G. Cavalieri, and D. S. Henningson, “Forcing statistics in resolvent analysis: application in minimal turbulent Couette flow,” *J. Fluid Mech.* **908**, A32 (2021).
- [21] F. R. Amaral, A. V. G. Cavalieri, E. Martini, P. Jordan, and A. Towne, “Resolvent-based estimation of turbulent channel flow using wall measurements,” *J. Fluid Mech.* **927**, A17 (2021).
- [22] S. Symon, S. J. Illingworth, and I. Marusic, “Large-scale structures predicted by linear models of wall-bounded turbulence,” *J. Phys. Conf. Series* **1522**, 012006 (2020).
- [23] L. I. Abreu, A. V. G. Cavalieri, P. Schlatter, R. Vinuesa, and D. S. Henningson, “Spectral proper orthogonal decomposition and resolvent analysis of near-wall coherent structures in turbulent pipe flows,” *J. Fluid Mech.* **900**, A11 (2020).
- [24] T. Ellingsen and E. Palm, “Stability of linear flow,” *Phys. Fluids* **18**, 487–488 (1975).
- [25] M. T. Landahl, “A note on an algebraic instability of inviscid parallel shear flows,” *J. Fluid Mech.* **98**, 243–251 (1980).
- [26] G. Tissot, A. V. G. Cavalieri, and E. Mémin, “Stochastic linear modes in a turbulent channel flow,” *J. Fluid Mech.* **912**, A51 (2021).
- [27] M. Lee and R. D. Moser, “Spectral analysis of the budget equation in turbulent channel flows at high Reynolds numbers,” *J. Fluid Mech.* **860**, 886–938 (2019).
- [28] T. Kawata and T. Tsukahara, “Scale interactions in turbulent plane Couette flows in minimal domains,” *J. Fluid Mech.* **911**, A55 (2021).
- [29] P. Doohan, A. P. Willis, and Y. Hwang, “Minimal multi-scale dynamics of near-wall turbulence,” *J. Fluid Mech.* **913**, A8 (2021).
- [30] C. G. Hernández, Q. Yang, and Y. Hwang, “Generalised quasilinear approximations of turbulent channel flow: Part 2. Spanwise scale interactions,” *arXiv:2112.01972v1* (2021).
- [31] M. R. Jovanović and B. Bamieh, “Componentwise energy amplification in channel flows,” *J. Fluid Mech.* **534**, 145–183 (2005).
- [32] B. Barthel, X. Zhu, and B. J. McKeon, “Closing the loop: nonlinear Taylor vortex flow through the lens of resolvent analysis,” *J. Fluid Mech.* **924**, A9 (2021).
- [33] W. C. Reynolds and W. G. Tiederman, “Stability of turbulent channel flow, with application to Malkus’s theory,” *J. Fluid Mech.* **27**, 253–272 (1967).
- [34] R. D. Cess, “A survey of the literature on heat transfer in turbulent tube flow,” *Tech. Rep.* (1958).
- [35] J. C. del Álamo and J. Jiménez, “Linear energy amplification in turbulent channels,” *J. Fluid Mech.* **640**, 5–26 (2006).
- [36] P. Welch, “The use of fast Fourier transform for the estimation of power spectra: a method based on time averaging over short, modified periodograms,” *IEEE. Trans. Audio Electroacoust.* **15**, 70–73 (1967).

- [37] J. F. Gibson, F. Reetz, S. Azimi, A. Ferraro, T. Kreilos, H. Schrobsdorff, M. Farano, A. F. Yesil, S. S. Schütz, M. Culp, and T. M. Schneider, “Channelflow 2.0,” manuscript in preparation (2019).
- [38] M. Lee and R. D. Moser, “Direct numerical simulation of turbulent channel flow up to $Re_\tau \approx 5200$,” *J. Fluid Mech.* **774**, 395–415 (2015).
- [39] J. C. del Álamo and J. Jiménez, “Spectra of the very large anisotropic scales in turbulent channels,” *Phys. Fluids* **15**, L41–L44 (2003).
- [40] J. C. del Álamo, J. Jiménez, P. Zandonade, and R. D. Moser, “Scaling of the energy spectra of turbulent channels,” *J. Fluid Mech.* **500**, 135–144 (2004).
- [41] V. Gupta, A. Madhusudanan, M. Wan, S. J. Illingworth, and M. P. Juniper, “Linear-model-based estimation in wall turbulence: improved stochastic forcing and eddy viscosity terms,” *J. Fluid Mech.* **925**, A18 (2021).
- [42] Y. Hwang, “Statistical structure of self-sustaining attached eddies in turbulent channel flow,” *J. Fluid Mech.* **767**, 254–289 (2015).
- [43] L. N. Trefethen, A. E. Trefethen, S. C. Reddy, and T. A. Driscoll, “Hydrodynamic stability without eigenvalues,” *Science* **261**, 578–584 (1993).
- [44] P. J. Schmid and D. S. Henningson, *Stability and transition in shear flows* (Springer, 2001).
- [45] K. Rosenberg and B. J. McKeon, “Efficient representation of exact coherent states of the Navier-Stokes equations using resolvent analysis,” *Fluid Dyn. Res.* **51**, 011401 (2019).
- [46] A. Madhusudanan, S. J. Illingworth, and I. Marusic, “Coherent large-scale structures from the linearized Navier-Stokes equations,” *J. Fluid Mech.* **873**, 89–109 (2019).
- [47] S. B. Vadarevu, S. Symon, S. J. Illingworth, and I. Marusic, “Coherent structures in the linearized impulse response of turbulent channel flow,” *J. Fluid Mech.* **963**, 1190–1203 (2019).
- [48] P. Kuhn, J. S. Müller, S. Knechtel, J. Soria, and K. Oberleithner, “Influence of eddy viscosity on linear modeling of self-similar coherent structures in the jet far field,” *AIAA Scitech 2022 Forum*, 0460 (2022).
- [49] Y. Hwang, “Mesolayer of attached eddies in turbulent channel flow,” *Phys. Rev. Fluids* **1**, 064401 (2016).
- [50] J. B. Marston, G. Chini, and S. M. Tobias, “Generalized quasilinear approximation: application to zonal jets,” *Phys. Rev. Lett.* **116**, 214501 (2016).
- [51] B. F. Farrell and P. J. Ioannou, “Structure and spacing of jets in barotropic turbulence,” *J. Atmos. Sci.* **64**, 3652–3665 (2007).
- [52] J. B. Marston, E. Conover, and T. Schneider, “Statistics of an unstable barotropic jet from a cumulant expansion,” *J. Atmos. Sci.* **65**, 1955–1966 (2008).
- [53] V. L. Thomas, B. K. Lieu, M. R. Jovanović, B. F. Farrell, P. J. Ioannou, and D. F. Gayme, “Self-sustaining turbulence in a restricted nonlinear model of plane Couette flow,” *Phys. Fluids* **26**, 105112 (2014).
- [54] V. L. Thomas, B. F. Farrell, P. J. Ioannou, and D. F. Gayme, “A minimal model of self-sustaining turbulence,” *Phys. Fluids* **27**, 105104 (2015).
- [55] A. Zare, M. R. Jovanović, and T. T. Georgiou, “Colour of turbulence,” *J. Fluid Mech.* **812**, 636–680 (2017).